

# Assessing the impact of two independent direction-dependent calibration algorithms on the LOFAR 21-cm signal power spectrum

## And applications to an observation of a field flanking the North Celestial Pole

H. Gan<sup>1</sup>, F. G. Mertens<sup>2,1</sup>, L. V. E. Koopmans<sup>1</sup>, A. R. Offringa<sup>3,1</sup>, M. Mevius<sup>3</sup>, V. N. Pandey<sup>3,1</sup>,  
S. A. Brackenhoff<sup>1</sup>, E. Ceccotti<sup>1</sup>, B. Ciardi<sup>4</sup>, B. K. Gehlot<sup>1,5</sup>, R. Ghara<sup>6,7</sup>, S. K. Giri<sup>8</sup>, I. T. Iliev<sup>9</sup>, and S. Munshi<sup>1</sup>,

(Affiliations can be found after the references)

Received XXX, 2022; accepted XXX, 2022

### ABSTRACT

**Context.** Detecting the 21-cm signal from the Epoch of Reionisation (EoR) has been highly challenging due to the strong astrophysical foregrounds, ionospheric effects, radio frequency interference (RFI) and instrumental effects. Better characterisation of their effects and precise calibration are, therefore, crucial for the 21-cm EoR signal detection.

**Aims.** In this work, we introduce a newly developed algorithm DDECAL (Direction-Dependent Calibration) and compare its performance with an existing direction-dependent calibration algorithm, SAGECAL, in the context of the LOFAR-EoR 21-cm power spectrum experiment.

**Methods.** We process one night of data from LOFAR observed by the HBA system. The observing frequency ranges between 114 and 127 MHz, corresponding to the redshift from 11.5 and 10.2. The North Celestial Pole (NCP) and its flanking fields were observed simultaneously in this data set. We analyse the NCP and one of the flanking fields. While the NCP field is calibrated by the standard LOFAR-EoR processing pipeline, using SAGECAL for the direction-dependent calibration with an extensive sky model and 122 directions, for the RA 18h flanking field, DDECAL and SAGECAL are used with a relatively simple sky model and 22 directions. Additionally, two different strategies are used for the subtraction of very bright and far sources, Cassiopeia A and Cygnus A.

**Results.** The resulting estimated 21-cm power spectra show that DDECAL performs better at subtracting sources in the primary beam region due to the application of a beam model, while SAGECAL performs better at subtracting Cassiopeia A and Cygnus A. The analysis shows that including a beam model during the direction-dependent calibration process significantly improves its overall performance. The benefit is obvious in the primary beam region. We also compare the 21-cm power spectra results on two different fields. The results show that the RA 18h flanking field produces better upper limits compared to the NCP for this particular observation.

**Conclusions.** Despite the minor differences between DDECAL and SAGECAL due to the beam application, we find that the two algorithms yield comparable 21-cm power spectra on the LOFAR-EoR data after foreground removal. Hence, the current LOFAR-EoR 21-cm power spectrum limits are not likely to depend on the direction-dependent calibration method. For this particular observation, the RA 18h flanking field seems to produce improved upper limits ( $\sim 30\%$ ) compared to the NCP.

**Key words.** cosmology: dark ages, reionisation, first stars, early Universe; techniques: interferometric; methods: data analysis, observational, statistical;

## 1. Introduction

Observation of the 21-cm signal of neutral hydrogen from the Epoch of Reionisation (EoR) is one of the most promising tools to reveal the formation and evolution history of the Universe (Furlanetto et al. 2006; Morales & Wyithe 2010; Pritchard & Loeb 2012; Liu & Shaw 2020). Many experiments are designed to detect the 21-cm signal from the EoR, including global experiments that aim at measuring the sky-averaged spectrum of the 21-cm signal with a single receiver, such as EDGES<sup>1</sup> (Bowman et al. 2018), LEDA<sup>2</sup> (Greenhill & Bernardi 2012), PRIZM<sup>3</sup> (Philip et al. 2018) and SARAS<sup>4</sup> (Singh et al. 2017; Thekkepattu et al. 2021); and interferometric experiments that aim at measuring the spatial brightness-temperature fluctuations of the 21-cm signal with a radio interferometer,

such as GMRT<sup>5</sup> (Paciga et al. 2011, 2013), LOFAR<sup>6</sup> (van Haarlem et al. 2013; Patil et al. 2017; Mertens et al. 2020), MWA<sup>7</sup> (Bowman et al. 2013; Barry et al. 2019b; Li et al. 2019) and PAPER<sup>8</sup> (Parsons et al. 2012; Cheng et al. 2018; Kolopanis et al. 2019), as well as the second generation instruments, HERA<sup>9</sup> (DeBoer et al. 2017; HERA Collaboration et al. 2021) and SKA<sup>10</sup> (Mellema et al. 2013; Koopmans et al. 2015).

However, the detection of the 21-cm signal has been very challenging, because the observed measurements are contaminated by the astrophysical foregrounds that are about 4-5 orders of magnitude stronger than the expected 21-cm signal (Bowman et al. 2009; Mertens et al. 2018; Gan et al. 2022), ionosphere (Mevius et al. 2016; Vedantham & Koopmans 2016;

<sup>1</sup> Experiment to Detect the Global EoR Signature

<sup>2</sup> the Large aperture Experiment to detect the Dark Ages, <http://www.tauceti.caltech.edu/leda/>

<sup>3</sup> the Probing Radio Intensity at high Z from Marion

<sup>4</sup> Shaped Antenna measurement of the background RAdio Spectrum.

<sup>5</sup> Giant Metrewave Radio Telescope, <http://gmrt.ncra.tifr.res.in>

<sup>6</sup> Low-Frequency Array, <http://www.lofar.org>

<sup>7</sup> Murchison Widefield Array, <http://www.mwatelescope.org>

<sup>8</sup> the Donald C. Backer Precision Array for Probing the Epoch of Reionisation, <http://eor.berkeley.edu>

<sup>9</sup> Hydrogen Epoch of Reionisation Array, <http://reionization.org/>

<sup>10</sup> the Square Kilometer Array, <http://www.skatelescope.org>

Edler et al. 2021) and radio frequency interference (RFI; Of-  
fringa et al. 2012, 2019a), as well as instrumental effects (Of-  
fringa et al. 2019b). Hence, suppressing these effects during cal-  
ibration is crucial for detection (Barry et al. 2016).

The calibration of the LOFAR-EoR KSP (Key Science  
Project) data uses the sky-based calibration approach. The pro-  
cessing pipeline of data has been developed and improved over a  
decade (Yatawatta et al. 2013; Patil et al. 2016; Patil et al. 2017;  
Mertens et al. 2020; Mevius et al. 2022). Due to the wide field of  
view of LOFAR, the data need to be calibrated depending on di-  
rection to correct for different errors from the varying beam and  
ionospheric effects. This direction-dependent (DD) calibration  
step, in particular, has been carried out by SAGECAL (Yatawatta  
2011, 2015, 2019). While SAGECAL has shown excellent calibra-  
tion performance, no other DD-calibration code has yet been ap-  
plied to LOFAR-EoR data.

This study introduces a newly developed DD-calibration al-  
gorithm DDECAL (Direction-Dependent Calibration; van Diepen  
et al. 2018) and compares the performance of two DD-  
calibration algorithms, DDECAL and SAGECAL, in the context of  
LOFAR-EoR 21-cm power spectra. The two algorithms have  
some differences, especially in the application of beam and  
constraining of gain smoothness in frequency. These could re-  
sult in different calibration performance. To study the differ-  
ences between the two algorithms, we process one-night of  
raw data obtained with the LOFAR High-Band Antenna (HBA)  
system on an unexplored flanking field of the North Celestial  
Pole (NCP) following similar steps in the standard LOFAR-EoR  
pipeline (Patil et al. 2017; Mertens et al. 2020). We use two  
different DD-calibration algorithms, DDECAL and SAGECAL with a  
more limited sky model and fewer directions, compared to the  
current analysis of the NCP field. The goal of the paper is not  
to compare the two DD-calibration algorithms using an identical  
sky model, clustering and settings, but to test the full end-to-  
end processing in terms of the resulting power spectra when the  
current-best settings and models for both algorithms are used,  
within the limits of their implementation. The observation cov-  
ers the unexplored frequency range, from 114 to 127 MHz cor-  
responding to the redshift range  $z = 11.5 - 10.2$ , pointing at RA  
 $18^h$ , DEC  $+86^\circ$ .

For DD-calibration, we use fewer directions ( $\sim 20$ ) com-  
pared to the standard 122 directions used for the NCP analy-  
sis (Patil et al. 2017; Mertens et al. 2020). The DD-calibration  
step is performed by two algorithms, DDECAL and SAGECAL. Be-  
sides varying the calibration scheme, we also test a “peeling”  
scheme. The peeling scheme, first proposed by Noordam & Os-  
chmann (2004), calibrates and subtracts bright sources sequen-  
tially in decreasing order of brightness. In Gan et al. (2022),  
we found that residuals of two very far and bright sources, Cas-  
siopeia A and Cygnus A (Cas A and Cyg A, hereafter) may be  
one of the sources of the excess power in the 21-cm power spec-  
tra. In this work, we model and subtract these two bright sources  
separately from the full sky model to improve the calibration  
performance. Similar approaches have been taken for the bright  
sources in Patil et al. (2017); Gehlot et al. (2019); Mertens et al.  
(2020).

The paper is arranged as follows. In section 2, we describe  
the data and the observational setup. In section 3, the strategy  
of the DD-calibration with LOFAR is described in detail and we  
summarise the two DD-calibration algorithms, DDECAL and SAGE-  
CAL. Section 4 is dedicated to the description of the processing  
of LOFAR-EoR data. In section 5, we present DD-calibration  
results with different algorithms and strategies including resid-  
ual images and power spectra. Different gain smoothness con-

**Table 1.** Summary of observational details of L612832.

Observation ID	L612832
Observing project	LT5_009
Pointing ( <i>J2000.0</i> )	$18^h00^m00^s, +86^\circ00'00''$
Frequency range	113.8657-127.1469 MHz
Redshift range	11.54-10.23
Observation start time (UTC)	2017-10-02 17:33:16.0
Observation end time (UTC)	2017-10-03 05:11:04.1
Duration	41868.1 s ( $\sim 11.6$ h)
Sub-band width	183.1 kHz
Time, frequency resolution	
Before averaging	2 s, 3.05 kHz
After averaging	10 s, 61.035 kHz

straints between DDECAL and SAGECAL are discussed in more depth  
in subsection 5.2.3. In section 6, we summarise the results and  
conclude.

## 2. Observation

The data analysed in this work have been obtained by the LO-  
FAR High-Band Antenna (HBA) system (van Haarlem et al.  
2013). The observational details of the data are summarised  
in Table 1. The LOFAR-EoR KSP has two target fields: the  
NCP (Yatawatta et al. 2013) and a field centred on the bright  
compact radio source 3C196 (Bernardi et al. 2010). From the  
LOFAR observation Cycles 0 to 10, about 2450 hours (more  
than 100 nights) and  $\sim 1100$  hours of data have been collected  
on these two fields, respectively. Around 75% of the collected  
data are assumed to be of good quality. In later observation cy-  
cles, the main fields have a configuration with a target field in the  
centre surrounded by a hexagonal ring of six flanking fields. For  
the NCP field, flanking fields are at an angular distance of  $4^\circ$ .  
The observing configuration is shown in Fig. 1 with the core sta-  
tion FWHM ( $\sim 4.8^\circ$  at 120 MHz van Haarlem et al. 2013). The  
pointing directions of the NCP flanking fields are summarised  
in Table A.1. The flanking field data are collected in addition to  
the main field data to increase the data volume ( $\sim 6$  times that  
of the main field per observation) and build a deep and wide sky  
model for the NCP. In principle, observing six flanking fields en-  
ables one to lower the errors in the 21-cm power spectrum by a  
square root of seven for a fixed bandwidth. The frequency range  
was chosen based on the best results from Patil et al. (2017). A  
disadvantage is that by observing multiple fields on a fixed band-  
width, one will limit the range of bandwidth. Because the main  
field and flanking fields share the same or very similar RFI, iono-  
spheric environment and systematics, the flanking field data can  
be used for cross-checking the NCP results. The flanking field  
data are also useful for calibration, e.g. for constructing better  
sky models for the main field, improving ionospheric modelling  
and expanding the field of view for polarisation images (Patil  
et al. 2017).

So far, the two published LOFAR-EoR KSP upper limits on  
the 21-cm signal power spectra in (Patil et al. 2017; Mertens  
et al. 2020) are based solely on NCP observations. In this work,  
for the first time, we analyse one night data on one of the six  
NCP flanking fields from the LOFAR observation Cycle 5, the

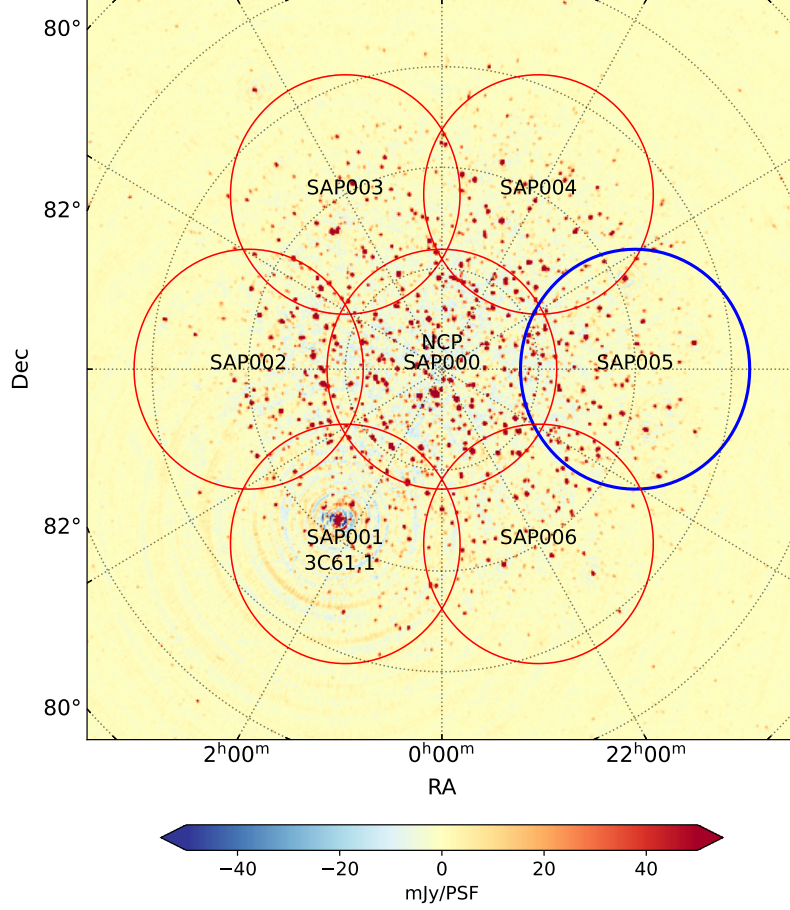


**Fig. 1.** Observing configuration of the NCP field in LOFAR-EoR. The main target field NCP is located in the centre and six flanking fields are distributed from the centre at an angular distance of  $4^\circ$  (marked with circles of radius  $4^\circ$ ). The bright radio source 3C61.1 is inside the RA 2h flanking field (SAP001). The image is constructed from a single observation night L612832 ( $\sim 11.6$ -hour long) using full sub-bands. In this work, we analyse one-night data on the RA 18h field (marked with a blue circle).

RA 18h flanking field (marked with a blue circle in Fig. 1). We create a new sky model on the chosen field, calibrate the data using the built sky model and estimate a 21-cm power spectrum. The 21-cm power spectrum is compared with the one on the NCP field for a cross-check.

While Patil et al. (2017) and Mertens et al. (2020) focused on the frequency range from 121.8 to 159.3 MHz (equivalently,  $z = 10.6 - 7.9$ ), we analyse the frequency range from 113.4 to 127.1 MHz, corresponding to a slightly higher redshift range from 11.5 to 10.2. We chose the RA 18h flanking field for analysis, because this field has never been analysed at this frequency range before. The data are obtained during nighttime to minimise ionospheric effects and avoid the sun, using all core stations and remote stations, with a spectral resolution of 3.05 kHz and a temporal resolution of 2 seconds. The observation duration is around 11.6 hours. The observational details are summarised in Table.1.

### 3. Direction-dependent calibration

The propagation of the signal from radio sources to the radio interferometer is often described by the Radio Interferometric Measurement Equation (RIME, Hamaker et al. 1996; Smirnov 2011). Considering an array of  $N$  elements, the correlation of signals between the  $i$ -th and  $j$ -th elements at frequency  $\nu$  and time  $t$  produces the observed visibility matrix  $\mathbf{V}_{ij\nu t}$ , which can

be described as

$$\mathbf{V}_{ij\nu t} = \mathbf{J}_{i\nu t} \mathbf{C}_{ij\nu t} \mathbf{J}_{j\nu t}^H + \mathbf{N}_{ij\nu t}, \quad (1)$$

where  $\mathbf{J}_{i\nu t}$  and  $\mathbf{J}_{j\nu t}^H$  are  $2 \times 2$  Jones matrices at frequency  $\nu$  and time  $t$  for element  $i$  and  $j$ .  $\mathbf{C}_{ij\nu t}$  is a  $2 \times 2$  coherency matrix of the intrinsic signal in a certain direction at the  $i$ -th and  $j$ -th elements (i.e., baseline  $ij$ ). The Jones matrices describe the electromagnetic interaction of the intrinsic signal, such as the instrumental effects including the beam shape and receiver response, and propagation effects including ionospheric distortions (Hamaker et al. 1996; Born et al. 1999).  $\mathbf{N}_{ij\nu t}$  is a  $2 \times 2$  noise matrix of baseline  $ij$ .

Due to the wide field of view of LOFAR<sup>11</sup>, LOFAR data need to be calibrated direction-dependently to compensate for different errors from varying beam and ionospheric effects. The sky model consists of many thousands of bright (a few Jy) and faint (a few mJy) discrete sources. These sources, therefore, need to be clustered to  $K$  directions for the direction-dependent (DD) calibration. Each cluster must have a sufficient integrated flux so that a DD gain solution can be obtained in a given time and frequency range with a high enough signal-to-noise ratio. The observed visibility matrix for elements  $i$  and  $j$  in Eq. (1) then

<sup>11</sup> The LOFAR core station field of view is  $\sim 17.73 \text{ deg}^2$  at 120 MHz (van Haarlem et al. 2013).

replaces the true sky with the sky model, becoming

$$\mathbf{V}_{ijvt} = \sum_{k=1}^K \mathbf{J}_{ikvt} \mathbf{C}_{ijkvt} \mathbf{J}_{jkvt}^H + \mathbf{N}_{ijvt}, \quad (2)$$

where  $k$  indicates the specific direction where gains are solved for. The goal of calibration is to estimate a set of parameters  $\theta$  describing the Jones matrices at a given time  $t$ , frequency  $\nu$  and element ( $i$  or  $j$ ) in Eq. (1). The solutions can either be applied to data to correct for the non-signal effects such as the ionosphere and instrumental errors, or the solutions predicted from a sky model can be subtracted from the data to calculate the residuals. Direction-independent (DI) gains are often applied to the data, whereas direction-dependent (DD) gains are used during the subtraction of the sky model.

The parameters  $\theta$  can be estimated by minimising the least-square's cost function

$$g(\theta) = \sum_{\nu, t, i, j} \left\| \mathbf{V}_{ijvt} - \sum_{k=1}^K \mathbf{J}_{ik}(\theta) \mathbf{C}_{ijkvt} \mathbf{J}_{jk}^H(\theta) \right\|^2. \quad (3)$$

In the calibration process, the gain solutions are assumed to be invariant over a small but finite time and frequency interval.

One of the main assumptions used for calibration is other effects including instrumental and ionospheric effects are intrinsically smooth as a function of frequency, while the 21-cm EoR signal is not. Enforcing spectral smoothness can, therefore, drastically improve the calibration performance by avoiding overfitting and signal suppression (Mouri Sardarabadi & Koopmans 2018; Mevius et al. 2022). Known spectrally unsmooth effects, such as RFI and cable reflections are handled by (RFI) excision or are treated as a DI bandpass error that can be solved at the DI-calibration step.

There are many calibration algorithms to solve the RIME in Eq. (2) (e.g. Kazemi et al. 2011; Kazemi & Yatawatta 2013; Tasse 2014; Ollier et al. 2018; Arras et al. 2019). In this work, we focus on two algorithms, DDECAL and SAGECAL, and compare their performance in the context of LOFAR-EoR 21-cm power spectra.

### 3.1. DDECAL

We use DDECAL as one of our DD-calibration tools in the analyses of this work. DDECAL is part of the `dp3` (Default Preprocessing Pipeline processing software; van Diepen et al. 2018)<sup>12</sup>. `dp3` performs streaming operations on an astronomical data set, such as flagging, averaging, calibration, compression, statistical and various other corrections. `dp3` is configured by providing a so-called parameter set (`parset`), which defines the operations to perform, as well as their parameters. DDECAL is implemented into `dp3` with the purpose of having a flexible framework to integrate constrained calibration algorithms. At present, it integrates four algorithms: a directional solving algorithm (Smirnov & Tasse 2015); a direction-iterative algorithm (Offringa et al. 2016); the Limited-memory Broyden–Fletcher–Goldfarb–Shanno (LBFGS) algorithm (Liu & Nocedal 1989; Yatawatta et al. 2019) and a hybrid algorithm that can combine methods. In this work, we have only used the directional-solving algorithm, which we will describe in the next section.

#### 3.1.1. Directional solving in DDECAL

In each iteration, the directional-solving algorithm finds the solution of all directions for a single element from the measurement equation of Eq. (1). It is an extension of the iterative single-directional solve algorithm (Mitchell et al. 2008; Salvini & Winholds 2014). If we define  $\mathcal{J}_i$  to be a matrix consisting of the  $2 \times 2$  matrices for element  $i$  and all the solved directions, stacked in the column direction:

$$\mathcal{J}_i = \begin{pmatrix} \mathbf{J}_{i,k=0} & \mathbf{J}_{i,k=1} & \mathbf{J}_{i,k=2} & \cdots \end{pmatrix}, \quad (4)$$

the solve algorithm finds the least-squares solution for  $\mathcal{J}_i$ , i.e., the calibration solutions for a single element but all directions at once:

$$\mathcal{J}_i = \underset{\mathcal{J}_i}{\operatorname{argmin}} \sum_{\nu, t, j} \left\| \mathbf{V}_{ijvt} - \sum_k \mathbf{J}_{ikvt} \mathbf{C}_{ijkvt} \mathbf{J}_{jkvt}^H \right\|^2. \quad (5)$$

During one iteration, the solutions for every element are calculated one by one and updated by moving the old value towards the new value, and this is iterated until convergence. This is the algorithm described by Smirnov & Tasse (2015).

To solve Eq. (5), we define matrices  $\mathcal{V}$  and  $\mathcal{M}$  that contain the multi-directional data visibilities and corrected model visibilities for one element. When we introduce an index symbol  $w$  that enumerates over all values of  $\nu$  and  $t$  inside the solution interval<sup>13</sup>, these two matrices can be defined by

$$\begin{aligned} \mathcal{V}_i &= \begin{pmatrix} \mathbf{V}_{i,j=0,w=0} & \mathbf{V}_{i,j=0,w=1} & \cdots & \mathbf{V}_{i,j=1,w=0} & \cdots \end{pmatrix}, \\ \mathbf{M}_{i,j,w,k} &= \mathbf{C}_{i,j,w,k} \mathbf{J}_{jk}^H, \\ \mathcal{M}_i &= \begin{pmatrix} \mathbf{M}_{i,j=0,w=0,k=0} & \mathbf{M}_{i,j=0,w=1,k=0} & \cdots & \mathbf{M}_{i,j=1,w=0,k=0} & \cdots \\ \mathbf{M}_{i,j=0,w=0,k=1} & \mathbf{M}_{i,j=0,w=1,k=1} & \cdots & \mathbf{M}_{i,j=1,w=0,k=1} & \cdots \\ \cdots & \cdots & \cdots & \cdots & \cdots \end{pmatrix}, \end{aligned} \quad (6)$$

where the columns of  $\mathcal{V}_i$  and  $\mathcal{M}_i$  enumerate all combinations of  $w$  and  $j$  (excluding  $i = j$ ), and the directions are stacked in the rows of  $\mathcal{M}_i$ . With these definitions, the solution to Eq. (5) is simplified to

$$\mathcal{V}_i = \mathcal{J}_i \mathcal{M}_i. \quad (7)$$

This results in a  $2 \times 2N_w N_a$  matrix  $\mathcal{V}_i$ , a  $2 \times 2N_d$  matrix  $\mathcal{J}_i$  and a  $2N_d \times 2N_w N_a$  matrix  $\mathcal{M}_i$ , with  $N_d$  the number of directions and  $N_w$  the number of timesteps  $\times$  frequencies inside the solution interval.

Eq. (7) is a standard linear equation, and  $\mathcal{J}_i$  can be solved for by standard linear algebra techniques such as using the normal equations  $\mathcal{J}_i = \mathcal{V}_i \mathcal{M}_i^H (\mathcal{M}_i \mathcal{M}_i^H)^{-1}$ , or QR-decomposition or singular-value decomposition of  $\mathcal{M}_i$ . DDECAL supports these three methods, and we have found that QR-decomposition generally results in a good compromise between accuracy and speed.

Besides the full Jones problem shown here, DDECAL has specialisations of this algorithm to find diagonal and scalar solutions, and can optionally constrain the algorithm to find phase-only or amplitude-only solutions, or solve for differential Faraday rotation.

<sup>12</sup> The source code for `dp3` can be found at <https://www.astron.nl/citt/DP3/>, and the `dp3` documentation can be found at <https://www.astron.nl/citt/DP3/>

<sup>13</sup>  $w$  loops over  $(\nu, t)$  for all possible solution intervals at a given direction  $k$  and element  $j$ .  $(\nu, t)$  alone indicates a solution at a certain interval.



### 3.1.2. Applying constraints to the algorithms

DDECAL allows the application of constraints on its four algorithms, including the directional-solving algorithm which is used in this paper. The implemented algorithms are written such that they iteratively step toward the solution. Updated solutions are used in the next iteration, leading again to more accurate solutions (as long as the algorithm converges), which repeats until the accuracy tolerance has been reached. Such iterative algorithms make it relatively easy to find constrained solutions: after moving the solutions towards the direction given by Eq. (7), a constraint can be applied.

DDECAL allows the application of different types of constraints, including spatial, temporal and spectral constraints. In this work, we use a constraint that forces the solutions to be spectrally smooth. DDECAL implements this by Gaussian smoothing the solutions with a requested width. When applying a spectral smoothness constraint, DDECAL calculates the next solution step independently for a number of channels, applies the smoothness constraint to all solutions simultaneously and then continues with the next iteration for each channel, repeating this until the channels simultaneously reach the stopping criterion.

### 3.2. SAGECAL

The space alternating generalised expectation maximisation (SAGE) algorithm (Fessler & Hero 1994; Kazemi et al. 2011) can be used to estimate the parameters describing  $\mathbf{J}_{ik}$  for all possible values of  $i$  and  $k$  in Eq. 2.

#### 3.2.1. SAGE algorithm

The ‘expectation’ step of the SAGE algorithm calculates the effective observed data along the  $m$ -th direction in a finite time interval, using

$$\mathbf{V}_{ijmv} = \mathbf{V}_{ijv} - \sum_{k=1, k \neq m}^K \hat{\mathbf{J}}_{ikv} \mathbf{C}_{ijkv} \hat{\mathbf{J}}_{jkv}^H, \quad (8)$$

where  $\hat{\mathbf{J}}_{ikv}$  and  $\hat{\mathbf{J}}_{jkv}^H$  are the estimated Jones matrices. The ‘maximisation’ step minimises the objective function only for the  $m$ -th direction defined under a Gaussian noise model as

$$g_{mv}(\mathbf{J}_{1mv}, \mathbf{J}_{2mv}, \dots) = \sum_{i,j} \left\| \mathbf{V}_{ijmv} - \mathbf{J}_{imv} \mathbf{C}_{ijmv} \mathbf{J}_{jmv}^H \right\|^2. \quad (9)$$

Using the SAGE algorithm, Eq. 2 can be simplified from a simultaneous calibration along  $K$  directions to  $K$  single direction sub-problems (Kazemi et al. 2011; Yatawatta 2016). For simplicity, below, we consider the calibration along one direction only and drop the subscript  $m$ , such that Eq. 9 becomes

$$g_v(\mathbf{J}_v) = \sum_{i,j} \left\| \mathbf{V}_{ijv} - \mathbf{A}_i \mathbf{J}_v \mathbf{C}_{ijv} (\mathbf{A}_j \mathbf{J}_v)^H \right\|^2, \quad (10)$$

where  $\mathbf{J}_v$  is Jones matrices for all elements along the  $m$ -th direction and  $\mathbf{A}_i$  is the canonical selection matrix to choose  $i$ -th element among  $N$  elements,

$$\mathbf{J}_v \triangleq [\mathbf{J}_{1mv}^T, \mathbf{J}_{2mv}^T, \dots, \mathbf{J}_{Nmv}^T]^T, \quad (11)$$

$$\mathbf{A}_i \triangleq [\mathbf{0}, \mathbf{0}, \dots, \mathbf{I}, \dots, \mathbf{0}],$$

where only the  $i$ -th matrix of  $\mathbf{A}_i$  is an identity matrix divided in time or frequency in Eq. 11.

### 3.2.2. Applying constraints to solutions

An observation with  $P$  data sets is distributed over  $C$  compute agents (typically,  $P \gg C$ ). Each data set has several frequency channels and each channel can be identified by its central frequency. Given that all known effects are spectrally smooth, SAGECAL constrains the continuity of  $J_v$  over frequency to improve the calibration performance by applying the consensus alternating direction method of multipliers algorithm (C-ADMM; Boyd et al. 2011; Yatawatta 2015, 2016). The objective function in Eq. 10 is then modified to an augmented Lagrangian with a regularisation parameter to guide solutions to approach the smooth regularisation function of choice  $\mathbf{B}_v \mathbf{Z}$ ,

$$\mathcal{L}_v(\mathbf{J}_v, \mathbf{Z}, \mathbf{Y}_v) = g_v(\mathbf{J}_v) + \|\mathbf{Y}_v^H (\mathbf{J}_v - \mathbf{B}_v \mathbf{Z})\| + \frac{\rho}{2} \|\mathbf{J}_v - \mathbf{B}_v \mathbf{Z}\|^2, \quad (12)$$

where  $\mathcal{L}_v$  denotes the Lagrange multiplier and the continuity of frequency is constrained by the frequency model described by a set of basis functions  $\mathbf{B}_v$ . SAGECAL uses third order Bernstein polynomials (Farouki & Rajan 1988) as the basis functions (Yatawatta 2019).  $\mathbf{Z}$  is a global variable shared by all frequencies in the data. The  $n$ -th ADMM iteration solves Eq. 12 in the following three steps for all frequencies in parallel:

$$(\mathbf{J}_v)^{n+1} = \arg \min_{\mathbf{J}_v} \mathcal{L}_v(\mathbf{J}_v, (\mathbf{Z})^n, (\mathbf{Y}_v)^n), \quad (13)$$

$$(\mathbf{Z})^{n+1} = \arg \min_{\mathbf{Z}} \sum_v \mathcal{L}_v((\mathbf{J}_v)^{n+1}, (\mathbf{Z}), (\mathbf{Y}_v)^n), \quad (14)$$

$$(\mathbf{Y}_v)^{n+1} = (\mathbf{Y}_v)^n + \rho((\mathbf{J}_v)^{n+1} - \mathbf{B}_v (\mathbf{Z})^{n+1}), \quad (15)$$

where the superscript  $(\cdot)^n$  denotes the  $n$ -th iteration and  $\rho$  is a regularisation parameter that determines the level of smoothness in frequency for each iteration. For our observation,  $\rho \sim 1000$  is found to be optimal for 30 ADMM iterations. For more discussions about the selection of  $\rho$ , we refer readers to Yatawatta (2015, 2016); Mertens et al. (2020); Mevius et al. (2022).

### 3.3. Differences between DDECAL and SAGECAL

Mathematically, both DDECAL and SAGECAL find gain solutions by minimising the least square’s cost function given by Eq. 3. Their detailed implementations, however, are different.

In this work, DDECAL applies the direction-solving algorithm to find solutions for all directions at a given element (i.e. an antenna), while SAGECAL applies the SAGE algorithm to find solutions for all elements at a fixed direction.

The frequency smoothness of gains is constrained differently in the two methods. DDECAL smooths gains by convolving them with a Gaussian kernel of a chosen bandwidth during each iteration of the optimisation, while SAGECAL uses an augmented Lagrangian with a regularisation parameter to enforce the gain smoothness.

Another important difference between DDECAL and SAGECAL is the application of beam. DDECAL supports the LOFAR HBA station beam (with usebeammodel in dp3), for that reason, an intrinsic sky model is used for calibration. SAGECAL currently does not support the LOFAR station beam model<sup>14</sup>. Hence, an apparent sky model (which folds the average beam into the sky model) is used for calibration.

<sup>14</sup> The latest version of SAGECAL only supports the LOFAR dipole beam model, in the future, more beam options will be supported; <http://sagecal.sourceforge.net/>

In theory, DD-calibration is supposed to solve gains for an optimal number of directions and solution intervals to take care of beam variations and ionospheric phase shifts. However, this process is not perfect and there are errors. In this work, DDECAL uses an intrinsic sky model with an HBA beam model, while SAGECAL uses an apparent model without a beam model. We focus on how these differences affect the results of DD-calibration and 21-cm signal power spectra.

## 4. Outline of the data processing

The observed data are processed on the dedicated high performance computing (HPC) cluster DAWN which consists of 124 NVIDIA K40 GPUs (Patil et al. 2017; Pandey et al. 2020). Because we are analysing data on a flanking field of the NCP and our main purpose is to compare the performance of two different DD-calibration algorithms, we use a slightly different data processing strategy from the LOFAR-EoR data processing pipeline adopted in Patil et al. (2017); Mertens et al. (2020), especially for the DI and DD-calibration steps. The main processing steps in this work are: (1) Pre-processing including data averaging and RFI flagging, (2) self-calibration iterations and imaging to create a sky model, (3) averaging and DI-calibration to correct the flux of sources, (4) DD-calibration with the two different algorithms described in Subsections 3.1 and 3.2 to subtract the sky model, (5) imaging, (6) visibility cube conversion, (7) residual foreground removal and (8) power spectrum estimation. Fig. 2 shows an overview of the RA 18h flanking field data processing pipeline of this work. Each step will be described in more detail in the following.

### 4.1. Pre-processing

RFI-flagging is performed by AOFLAGGER (Offringa et al. 2012) on the highest time and spectral resolution of 2 seconds and 3.05 kHz (64 channels per sub-band, 183 kHz). In this step, the four edge channels 0, 1, 62 and 63 of sub-bands are flagged to avoid aliasing effects from the poly-phase filter (Patil et al. 2017). After the first RFI-flagging, the remaining 60 channels are averaged to 15 channels (12.2 kHz per channel) and the data are archived in the LOFAR LTA at SURFsara in Amsterdam and Poznan in Poland (Mertens et al. 2020). On this averaged data, we perform a second RFI flagging and subsequently the data are averaged to three channels (61 kHz per channel) per sub-band and 2 seconds resolution. This initial RFI-flagging results in a  $\sim 5\%$  loss of the LOFAR-EoR HBA data (Offringa et al. 2013). This pre-processing step is identical to the one in the standard LOFAR-EoR pipeline (Mertens et al. 2020).

### 4.2. Direction-independent calibration

The first step of calibration begins with a self-calibration (Cornwell & Wilkinson 1981; Pearson & Readhead 1984) and the main goal is to correct the source fluxes and build up a sky model for the DD-calibration. We perform a first gain calibration on the averaged visibilities with a sky model consisting of 355 bright point sources from the NCP sky model. The gain calibration is carried out by GAINCAL in dp3. Using `usebeammodel` option in GAINCAL, we apply the LOFAR-HBA beam model during calibration and use the initial sky model with intrinsic fluxes. To reduce the data volume and accelerate the calibration process, we first average the data to a 10-second time resolution and gain solutions are calculated on the same time scale per sub-band with

the LOFAR-HBA beam model.<sup>15</sup> Note that baselines are not limited during the first DI-calibration of self-calibration. Based on our test, if we use the same  $50\lambda$  cut both for self-calibration and the subsequent DI-calibration, data on baselines close to the  $50\lambda$  cut are not well calibrated. For this reason, we decided not to apply a baseline cut when creating a sky model (during self-calibration). The  $50\lambda$  cut is applied during DI-calibration after the self-calibration step. We combine all 69 sub-bands and limit baselines up to  $10000\lambda$  to create a high resolution image with a pixel size of 6 arcsec. The calibrated visibilities are imaged and deconvolved by the multiscale CLEAN feature of WSCLEAN (Offringa et al. 2014; Offringa & Smirnov 2017). The obtained CLEAN components are saved as two types of sky models: an apparent model and an intrinsic model. The sources in the apparent model are attenuated by the average beam. The two models will be used in the next calibration steps with combinations of two DD-calibration algorithms. DDECAL can apply the LOFAR-HBA beam model in calibration and so we can use an intrinsic sky model. SAGECAL requires an apparent sky model, because the beam model is not applied.

At this stage, we compare the intrinsic flux of four known bright sources (J190401.7+8536, 6C B184741+851139, 6C B174711+844656 and 6C B163113+855559) around the phase centre (ideally, within  $\sim 4.75^\circ$ , being the FWHM of the LOFAR core stations at 120 MHz; van Haarlem et al. 2013) to the ones from catalogues to check whether their fluxes match. The details of sources used for flux scaling and their catalogues are summarised in Table.B.1. We aim for the intrinsic flux calibration accuracy of 10% or better. An additional calibration factor is applied to match the intrinsic sky model to the catalogue fluxes. Finally, we perform a DI-calibration using the extended CLEAN component model on the pre-processed data. It is similar to the first DI-calibration step. The data is first averaged to a 10-second time resolution and the CLEAN component model (intrinsic) is used with the LOFAR-HBA beam model. Baselines are limited to  $50\text{--}9500\lambda$  this time. The lower baseline cut is applied to avoid the diffuse emission (Patil et al. 2017), while the upper baseline cut comes from the constraint (of  $10000\lambda$ ) of the sky model.

### 4.3. Direction-dependent calibration

After we have created the new sky model and re-scaled the flux in the DI-calibration step, we perform a DD-calibration. The main goal is to subtract sources in the sky with their DD-calibration gains. In this work, we perform this task with two different DD-calibration algorithms, DDECAL and SAGECAL, described in Subsections 3.1 and 3.2. Because Cas A and Cyg A are very bright and far away from the phase centre and their solutions can be distinctive from ones of the remaining sources close to the phase centre. Hence, they need to be calibrated in a separate cluster, similar to the approach used for calibrating the bright source 3C61.1 in the NCP field by Patil et al. (2017) and Mertens et al. (2020). Hence, we test two methods for the subtraction of the sky model: (1) the 1-step method: the CLEAN component model with a Cas A and Cyg A model are divided into 22 clusters (20 clusters for the CLEAN model and one cluster each for Cas A and Cyg A), and all the sources are predicted and sub-

<sup>15</sup> In the standard LOFAR-EoR pipeline, the DI-calibration is conducted on the high resolution data, before averaging. We also performed a test on calibrating the higher resolution data before averaging, but the results were almost identical to the one after averaging. In this case, calibrating on the higher resolution increases the computing time by a factor of 4-5 without a significant improvement. Hence, in this work, we decide to calibrate the data after averaging.

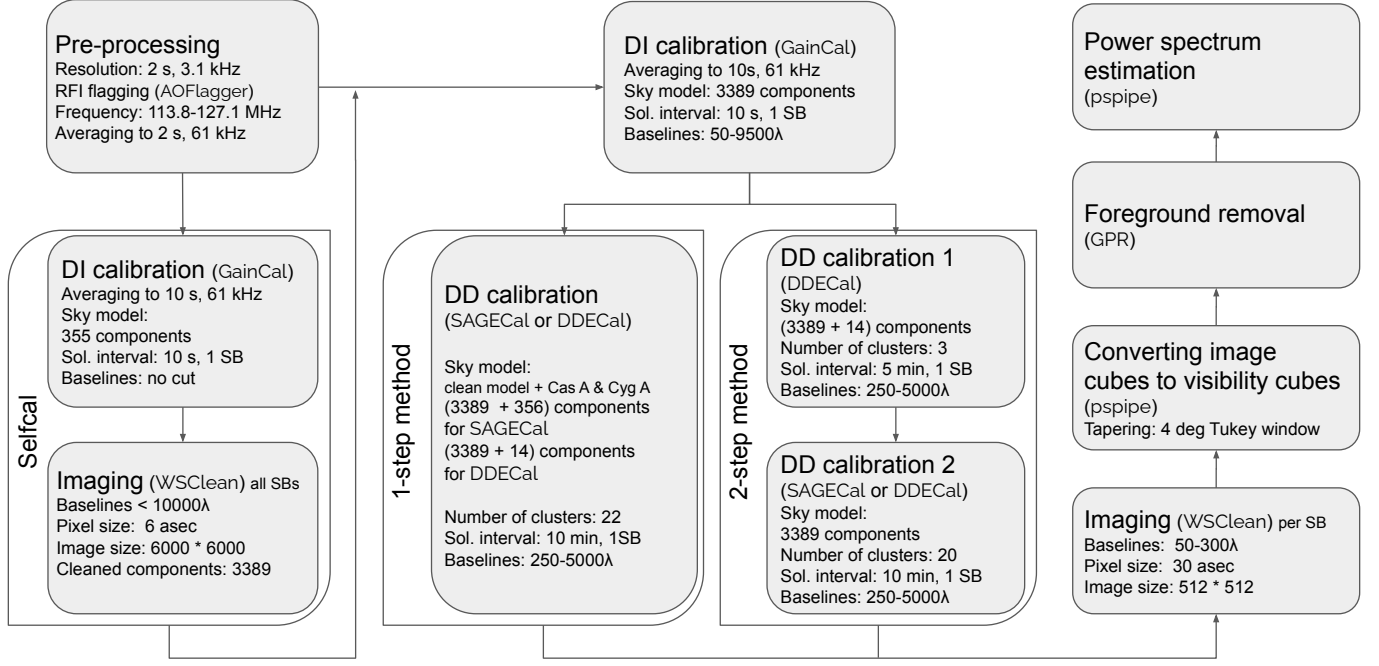


**Fig. 2.** Processing pipeline of the LOFAR-EoR flanking field data in this work to obtain the 21-cm power spectra with two different DD-calibration algorithms. The pipeline is slightly different from the standard LOFAR-EoR HBA processing pipeline in (Pandey et al. 2020; Mertens et al. 2020) because our main purpose is comparing the performance of two DD-calibration algorithms. We also adopt two different clustering approaches for the DD-calibration, i.e. the 1-step and 2-step methods, to investigate how different clustering impacts the subtraction of the sky model.

tracted simultaneously in one step; (2) the 2-step method: the CLEAN model, Cas A and Cyg A are divided into 3 clusters, respectively. Cas A and Cyg A are predicted and subtracted first, after which the CLEAN model is again divided into 20 clusters, predicted and subtracted from the data. Solutions are calculated for 10-min time intervals and each sub-band for the two DD-calibration algorithms and two different approaches to subtracting the sources.

We adopt the same baseline cut applied in the standard LOFAR-EoR pipeline, i.e. 250-5000 $\lambda$ . The lower baseline cut is used to reduce signal suppression on the baselines of 50-250 $\lambda$  used for the 21-cm signal power spectrum extraction, avoid the effects from the diffuse emission and include enough baselines for the required S/N ratio. The upper baseline cut is applied to avoid sky model error and ionospheric phase fluctuations on longer baselines leaking into the short baseline gain solutions (Patil et al. 2016; Mertens et al. 2020; Mevius et al. 2022).

#### 4.4. Imaging and conversion to brightness temperature

After DI and DD-calibration, imaging, removal of residual foreground and power spectrum estimation are similar to the standard LOFAR-EoR pipeline (see Mertens et al. 2020, for more details). The residual visibilities after the DD-calibration are gridded and imaged per sub-band to create an image cube using wsclean. We adopt identical imaging parameters used by Mertens et al. (2020), a Kaiser-Bessel anti-aliasing filter with a kernel size of 15 pixels, an oversampling of 4096 and 32 w-layers. According to Offringa et al. (2019b), these parameters are chosen to confine the systematics from gridding below the predicted 21-cm signal.

At this stage, we create even and odd 10-second time-differenced images to estimate the thermal noise of the data. We estimate the thermal noise for the NCP and RA 18h flanking field, and use them for the flux scale cross-check. The power spectrum is corrected by a factor of two downwards to account for the increase in noise level due to the differencing. The results are discussed in more detail in the following section.

The image cube with a field of view of  $12^\circ \times 12^\circ$  and a pixel size of 0.5 arcmin is then multiplied by a Tukey function with a diameter of  $4^\circ$  to concentrate on the beam centre. The image cube has units of Jy/PSF. For estimating the power spectrum, the image cube is spatially Fourier transformed into a gridded visibility cube and converted to units of Kelvin, as described in Offringa et al. (2019b).

#### 4.5. Foreground removal and power spectrum estimation

The remaining foregrounds in the residual Stokes-I visibilities are further removed by the Gaussian Process Regression (GPR) foreground removal technique (Mertens et al. 2018; Mertens et al. 2020). GPR enables a separation between different components in observations including smooth astrophysical foregrounds, mode-mixing contaminants, noise and the 21-cm signal by modelling each of them as a Gaussian Process (GP), assuming they can be described by Gaussian processes to first order. GPR properly accounts for degeneracies between the signal components, by marginalising other components.

Finally, the variations of the 21-cm signal as a function of wavenumber  $k$  (at different scales) are obtained by a power spectrum. It is estimated by taking the Fourier transform of the foreground-subtracted visibility cube in the frequency direction and converting angle and frequency, to comoving distances (Morales & Hewitt 2004; McQuinn et al. 2006).

**Table 2.** The parameter setup for the multiscale deconvolution algorithm with WSCLEAN.

Parameter	Value
Pixel scale	6 arcsec
Briggs weighting	0.0
Baselines	$< 10000\lambda$
Fitting spectra*	3 terms
Auto mask	$7\sigma$
Final threshold	$3\sigma$

**Notes.** \*WSCLEAN has an option to enforce a smooth spectrum during joined channel deconvolution by fitting a polynomial. In this work, we fit a polynomial with 3 terms (i.e., a second-order polynomial) to achieve a smooth spectrum.

We can average the power spectrum in  $k$ -bins to create the spherically-averaged dimensionless power spectrum or define the cylindrically-averaged power spectrum, as a function of angular  $k_{\perp}$  versus line-of-sight  $k_{\parallel}$ .

## 5. Results

In this section, we present the results of processing one night observation from LOFAR-EoR with DDECAL and SAGECAL. We present the results of each processing step, following the data processing pipeline introduced in section 4. We also compare differences in their performance in terms of removing sources in subsections 5.2-5.4. In section 5.5, we compare sky images, power spectra and upper limits on the RA 18h flanking field and NCP field.

### 5.1. The RA 18h flanking field sky model and DI-calibration

The sky model of the RA 18h flanking field is built by the multiscale deconvolution algorithm of WSCLEAN with the parameters listed in Table.2. The intrinsic flux of the CLEAN model is then scaled to match the fluxes of the four bright sources around the phase centre listed in Table.B.1 at the central observing frequency 119.725 MHz with a spectral index  $\alpha = -0.6$ . With a flux scaling factor 1.91, we find a mean ratio of 0.997 between the intrinsic CLEAN flux and the references with a standard deviation of 0.0861. In addition, we compare the estimated thermal noise on the RA 18h flanking field and NCP (scaled by NVSS J011732+892848 Patil et al. 2017; Mertens et al. 2020) from the same observation. Their estimated thermal noise should closely match if the absolute flux scale is performed accurately. The average ratio of the estimated thermal noise between the NCP and RA 18h flanking field is found to be 1.06, showing that the absolute flux scaling is well performed and the estimated thermal noise values on the two fields are comparable. Note that due to the  $4^\circ$  difference in pointing, the sensitivity is slightly different between the two fields. The noise in part is set by the total power in the beam, which is also partly contributed by sources in the field and diffuse emission. Hence, a perfect flux agreement is not expected. The top panel of Fig.4 shows images of the RA 18h flanking field after DI-calibration.

### 5.2. Direction-dependent gain calibration

In the DD-gain calibration step, we cluster the sky model into a number of directions, predict visibilities in each direction and

subtract the clustered sky model sources with their DD-gain applied from the data. An example of the obtained DD-gain power spectra for one station is presented in Appendix.E. In this subsection, we will discuss the sky model we use for the DD-calibration and compare its performance using two algorithms, DDECAL and SAGECAL, and two different approaches regarding the subtraction of Cas A and Cyg A.

#### 5.2.1. Clustering of the sky model

The 3389 CLEAN components after self-calibration are clustered into 20 directions identically for the two algorithms as shown in Fig. 3. We make sure that clustering does not contribute to the DD-calibration difference between the two algorithms. The detailed clustering information of the sky model is summarised in Table.B.2 and the differences between the two sky models are summarised in Table.3. Finally, we add Cas A and Cyg A into the two sky models, as these bright radio sources, even located outside the field of view, will enter via side-lobes and leave residuals in the power spectrum if not included in the sky model (Patil et al. 2017; Mertens et al. 2020). For DDECAL, we use the Cas A and Cyg A model (14 components) from the low resolution A-team sky model<sup>16</sup>. For SAGECAL, we use shapelet models created from wide-band LOFAR-LBA and HBA observations with  $\sim 350$  components (Yatawatta 2011)<sup>17</sup>. The additional Cas A and Cyg A components are clustered into their respective directions.

#### 5.2.2. Images

In Fig. 4, we show  $5^\circ \times 5^\circ$  images of the Stokes-I residuals after DD-calibration with four different scenarios using DDECAL and SAGECAL (middle and bottom). Compared to the Stokes-I images before DD-calibration in Fig. 4 (top), most bright sources are removed well after DD-calibration in Fig. 4 (middle and bottom). In the primary beam region, DDECAL (middle left and bottom left in Fig. 4) removes more power compared to SAGECAL (middle right and bottom right in Fig. 4) for both 1-step and 2-step methods.

However, depending on the strategy, there are some differences in their residuals. In Fig. 4, the images calibrated by DDECAL (middle left and bottom left) have more compact residual sources than the images calibrated by SAGECAL (middle right and bottom right). Notably, DDECAL shows better performance with the 1-step method in the primary beam region and the residual power is lower with the 1-step method (middle left) than with the 2-step method (bottom left). The difference between the 1-step and 2-step methods is marginal for SAGECAL (middle right and bottom right).

We choose a reference source close to the centre to compare the residuals after DD-calibration with the four scenarios. The reference source is marked with a dashed blue circle in Fig. 4. The flux of the source is largely reduced after DD-calibration in all four scenarios. DDECAL shows an over-subtraction where the source appears as negative (in blue). The over-subtraction is stronger in the 2-step method than in the 1-step method. On the other hand, the residuals of SAGECAL are rather positive (in

<sup>16</sup> <https://github.com/lofar-astron/prefactor/tree/master/skymodels>

<sup>17</sup> We also tested the calibration performance with a high resolution Cas A and Cyg A sky model with more components with DDECAL. However, using more components did not significantly improve the subtraction of the sources. Hence, we decide to use the low resolution model to reduce the computing time.

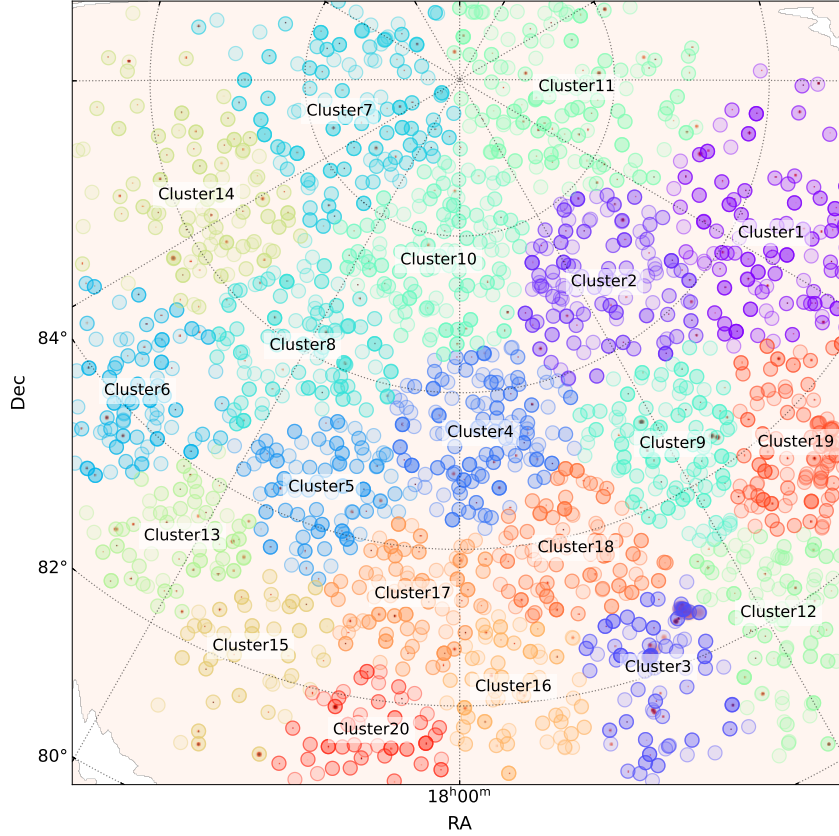


**Fig. 3.** The flanking field sky model from CLEAN components with the LOFAR beam applied clustered into 20 directions for the DD-calibration. Different colours denote different solving directions. Each cluster has an angular radius of  $1 - 2^\circ$ .

**Table 3.** The sky model setups for DDECAL and SAGECAL.

Parameter	DDECAL	SAGECAL
CLEAN model flux	intrinsic	apparent
Beam	applied	not applied
Frequency smearing correction	not applied	applied
Time smearing correction	not applied	applied
Number of clusters	20	
Number of components	3389	
Cas A & Cyg A model	Gaussian & point sources	shapelet sources
Number of clusters	2	
Number of components	14	$\sim 350$

red) and not as compact as ones from DDECAL. Difference images between the DD-calibration scenarios subtracted by the DDECAL and 1-step scenario (middle left) are shown in Fig.C.1.

Overall, DDECAL shows better performance than SAGECAL in the primary beam region, especially when carried out by the 1-step method. This difference between DDECAL and SAGECAL may be explained by the application of the LOFAR-HBA beam in DDECAL which enables more realistic prediction and subtraction of visibilities.

In principle, the number of directions and the time or frequency interval of solutions in DD-calibration are chosen to naturally capture the direction-dependent effects including beam

variations and ionospheric phase fluctuations etc. However, this calibration process is not perfect (e.g., due to the incomplete sky model or bad choice of solution intervals) and there are errors. Increasing the solution resolution, i.e., using a finer time or frequency interval for solutions, can be useful for capturing rapid varying beam variations and ionospheric fluctuations to a certain extent, however, it could also introduce extra noise into data and add extra structures in time and frequency. This point is also partially shown in Fig. E.4 where we use different time intervals, 5 min and 10 min, to calibrate Cas A and Cyg A. The 5 min interval results (bottom panel) did not show an improvement compared to the 10 min interval results (second panel). What we



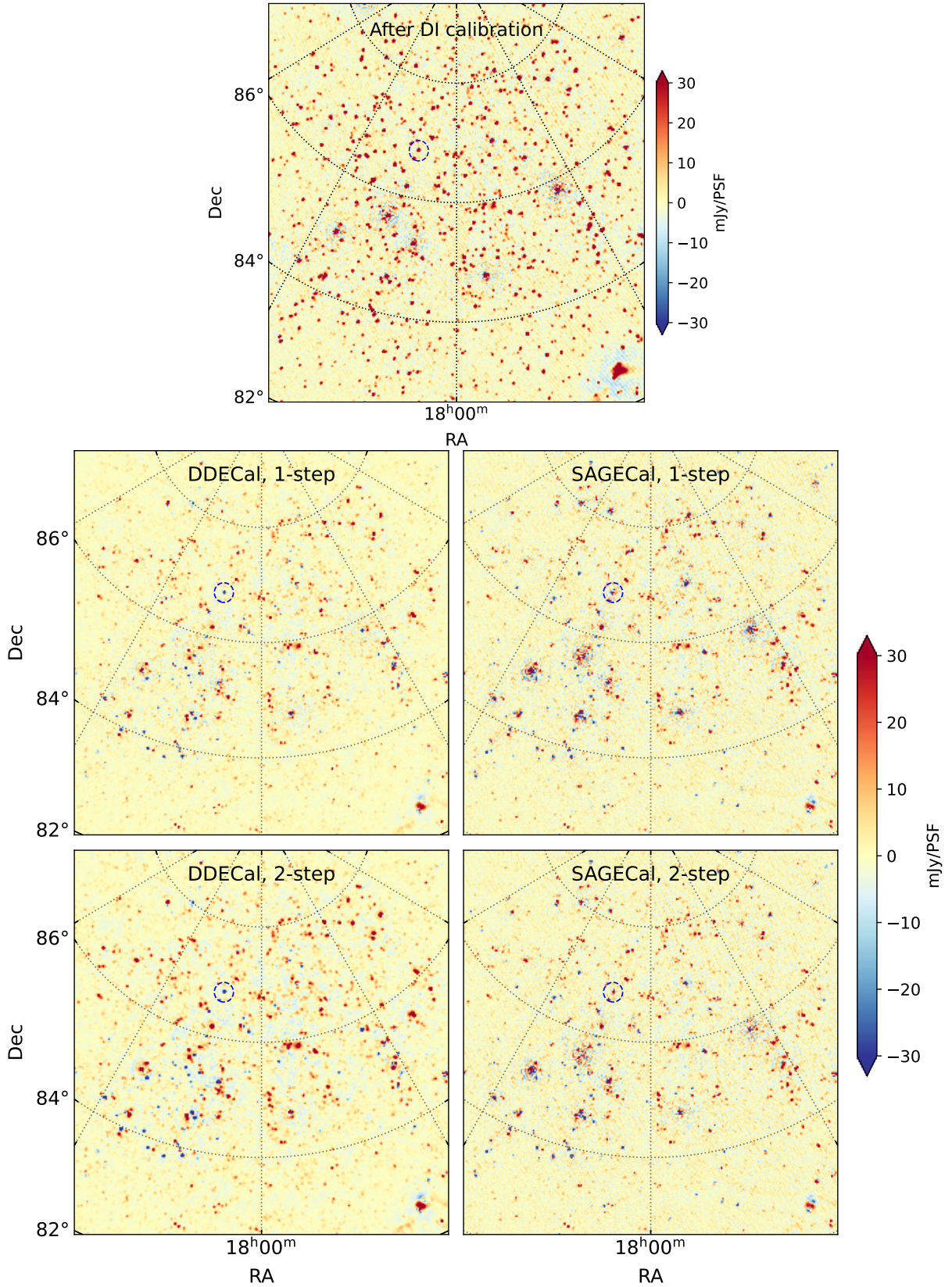


**Fig. 4.** LOFAR-HBA  $5^\circ \times 5^\circ$  Stokes-I residual images after DI- and DD-calibration with four different calibration scenarios on the RA 18h flanking field at frequency 113.9-127.1 MHz. The images are created with a pixel size of 0.2 arcmin using baselines 50 – 5000 $\lambda$ , combining 69 sub-bands and a single observation night L612832 ( $\sim$  11.6-hour). **Top:** after DI-calibration. **Middle:** calibrated by DDECAL (left) and SAGECAL (right) with the 1-step method). **Bottom:** calibrated by DDECAL (left) and SAGECAL (right) with the 2-step method). Different DD-calibration scenarios also show different residuals. A source close to the centre is marked with a dashed blue circle as a reference. The residuals of the reference source look different in the four scenarios.



found in this work is that having a physical beam model during DD-calibration will improve the performance of calibration, especially, in the primary beam region.

To compare the subtraction performance of distant sources, such as Cas A and Cyg A, we create full sky Stokes-I residual images ( $120^\circ \times 120^\circ$ ) after DI-calibration and four different DD-calibration scenarios. The images are created by combining all sub-bands, integrating the full observation and applying 50–300  $\lambda$  baseline cut (comparable to the cut used for the power spectrum estimation later).

Fig. 5 shows the residual Stokes-I images after DI-calibration (top left), Cas A and Cyg A subtraction with DDECAL (bottom left) and DD-calibration with the four scenarios (second and third columns) on the RA 18h flanking field. By comparing the two images in the first column, before and after the subtraction of Cas A and Cyg A, we find that this extra step taken by DDECAL significantly reduces the power from Cas A and Cyg A without changing the power around the phase centre. The subtraction of Cas A and Cyg A is not as efficient with the 1-step DDECAL method (second panel on top) in Fig. 5), showing more residuals from Cas A and Cyg A after the DD-calibration compared to the other three scenarios.

This difference in the performance of the subtraction of Cas A and Cyg A between the 1-step and 2-step methods is very evident in DDECAL (second column in Fig. 5), but not as much in SAGECAL (last column in Fig. 5). It is still unclear why the 1-step method performs better in subtracting sources in the primary beam than the 2-step method for DDECAL in this specific case; and whether the existence of distant and bright sources (such as Cas A and Cyg A, in this case) in the sky model improves the prediction of nearby sources within the field of view.

However, this different performance of DDECAL between the 1-step and 2-step methods shows the importance of optimising parameters during the DD-calibration. With the same calibration algorithm and sky model, the calibration performance can be different, depending on the exact parameters we use and the order in which the directions are solved for.

The 1-step SAGECAL method shows the best subtraction of Cyg A compared to others, leaving the lowest power in the image (second panel on bottom in Fig. 5). One of the major differences between DDECAL and SAGECAL is the application of time and frequency smearing correction and this correction is only applied for SAGECAL in this work. The better Cas A and Cyg A subtraction of SAGECAL could be due to this smearing correction.

In the far field in Fig. 5, Cas A and Cyg A are by far, the most dominant sources of residuals, even after DD-calibration. This is in line with the previous study on sources of excess variance in the LOFAR-EoR 21-cm power spectra (Gan et al. 2022). The dominant imprint of Cas A and Cyg A maybe are contributors of the excess power in the wedge.

### 5.2.3. Gain smoothness difference in DDECAL and SAGECAL

One of the main differences between the two DD-calibration algorithms is the implementation of frequency smoothness constraints. As discussed in section 3, all sky signals, apart from the 21-cm signal are supposed to be smooth in frequency. By enforcing gains to be smooth in frequency, we can minimise signal suppression and avoid enhancing the noise variance introduced by calibration (Mevius et al. 2022). DDECAL enforces this gain smoothness by convolving solutions with a Gaussian kernel of a given size for each iteration.

We test two different kernel sizes, 1 MHz and 4 MHz, of which the 4 MHz kernel turns out to be better for the analy-

sis (i.e. better subtraction of the sky model). On the other hand, SAGECAL iteratively penalises solutions that deviate from a frequency smoothness prior by a quadratic term of a third-order Bernstein polynomial over the full bandwidth ( $\sim 13$  MHz in this case).

To understand the effects of different frequency constraints in DDECAL and SAGECAL, we compare the delay  $\tau$  transformed and peak-normalised (at  $\tau = 0$  ns) gains obtained by the two algorithms. Fig. 6 shows the normalised gains obtained by DDECAL (on top) and SAGECAL (on bottom) with the 2-step method for the first five clusters (from left to right) and core stations (in different colours) in delay space. For all clusters and stations, SAGECAL gain distributions show slightly narrower widths, compared to the ones from DDECAL. A more noticeable difference is shown in the tails of gains at large delays. Gains from DDECAL hit a noise floor ( $|G| \sim 10^{-4}$ ) at  $|\tau| > 1000$  ns, while gains from SAGECAL continue to drop. However, gains from DDECAL and SAGECAL have similar distributions in delay space, despite the difference in the flux of the sky model and application of the beam model. We assume that the different frequency constraints used in the two algorithms have comparable effects in this analysis.

### 5.3. Foreground removal: Gaussian process regression (GPR)

In this subsection, we show the results of the GPR foreground removal after the four different DD-calibration scenarios, respectively.

The residual foregrounds after the DD-calibration can be further removed by GPR. GPR models each component in observation as a Gaussian Process (GP; Rasmussen & Williams 2005). The parametric GP model has five components: the foreground residuals that are composed of intrinsic sky emission and mode mixing contaminants related to the chromaticity of the instrument and calibration errors; the 21-cm signal; the spectrally uncorrelated noise; and the spectrally correlated excess noise.

The modelled GP components are summarised for the four different DD-calibration scenarios in Table. 4. We refer readers to Mertens et al. (2020) for the detailed selection of the covariance model. GPR uses a Matern covariance function for modelling different components in the residuals. A Matern covariance function is defined with three hyperparameters,  $\eta$ ,  $\sigma$  and  $l$ . The parameter  $\eta$  constrains the smoothness of the function,  $\sigma^2$  is the variance and  $l$  is the spectral coherence scale of each component. Mertens et al. (2018) have found the most probable setting of GP and hyperparameter priors and the found values are used in this work.

We note that the coherence scales  $l$  converge to similar values, especially, for the excess noise and 21-cm signal components, i.e.,  $l_{\text{ex}}$  and  $l_{21}$ , given the four different DD-calibration scenarios. This is expected because the four scenarios are based on the same observation and the DD-calibration step should not bias the excess variance and 21-cm signal.<sup>18</sup> On the other hand, the intrinsic sky and mix coherence scales, i.e.,  $l_{\text{sky}}$  and  $l_{\text{mix}}$ , depend on the calibration method in Table. 4. For instant, DDECAL shows longer intrinsic sky coherence scales (i.e., 82–85 MHz) compared to SAGECAL (i.e., 39–41 MHz).

This again can be explained by the difference in the residuals after the application of DDECAL and SAGECAL. As we discussed earlier, due to the application of the beam model, DDECAL and

<sup>18</sup> The excess variance by definition is the extra noise that is above the thermal noise level and cannot be removed easily with DD-calibration or GPR (Mertens et al. 2018; Gan et al. 2022).

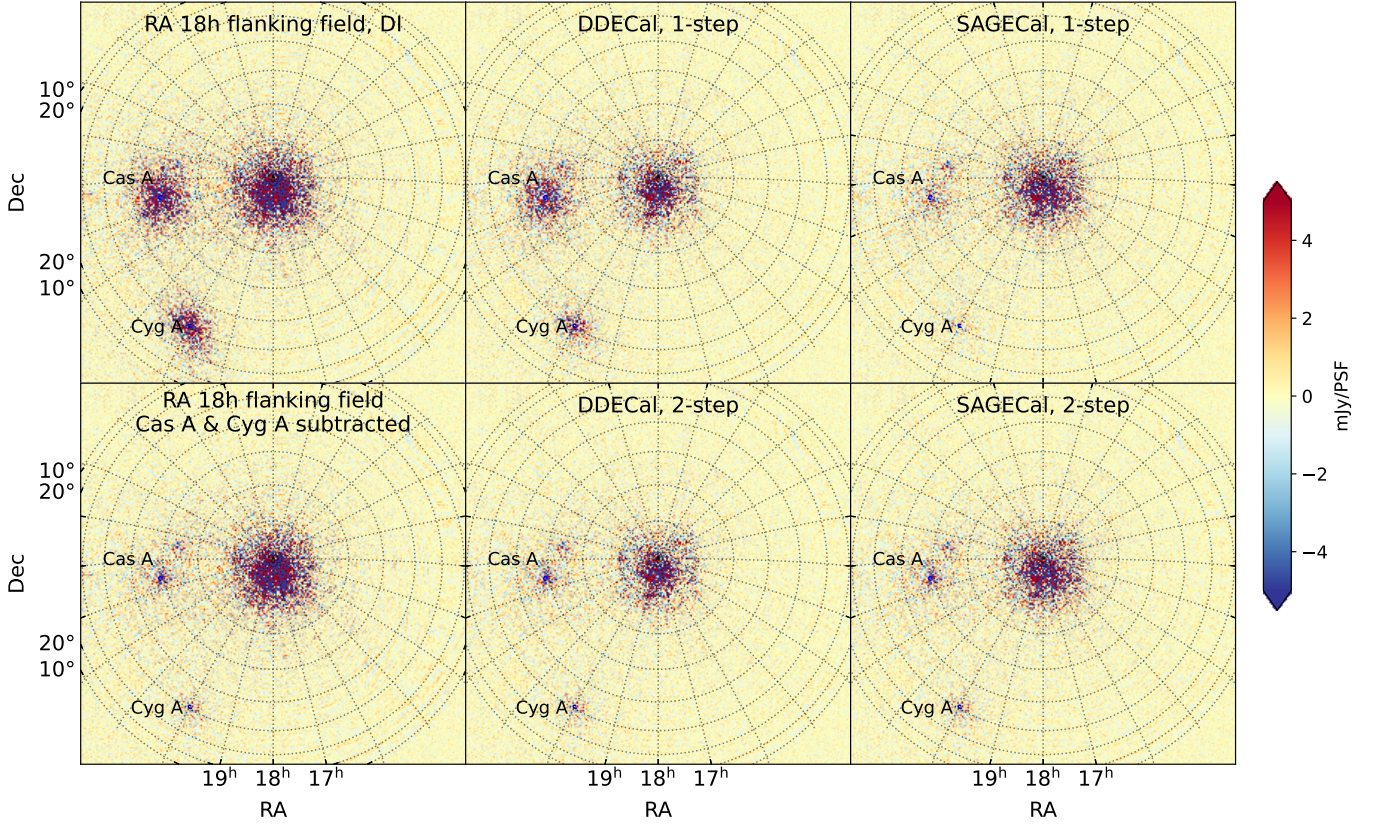


**Fig. 5.** Full sky ( $120^\circ \times 120^\circ$ ) Stokes-I residual images created by using 69 sub-bands and 50–300.1 baseline cut and integrating the full observation after DI-calibration, Cas A and Cyg A subtraction and DD-calibration with four different strategies with DDECAL and SAGECAL on the RA 18h flanking field. The top left image shows the residuals after DI-calibration (top left). After DI-calibration, we subtract all sources including Cas A and Cyg A in one step (i.e. the 1-step method, middle and right on top), or we first subtract Cas A and Cyg A (i.e., the 2-step method, bottom left) and subtract sources in the centre (middle and right on the bottom). The flux of Cas A and Cyg A is largely reduced after Cas A and Cyg A subtraction (bottom left), while sources in the centre remain. The 1-step method with SAGECAL shows comparable performance in Cas A and Cyg A subtraction (top right), while DDECAL still shows a high level of residuals (top middle).

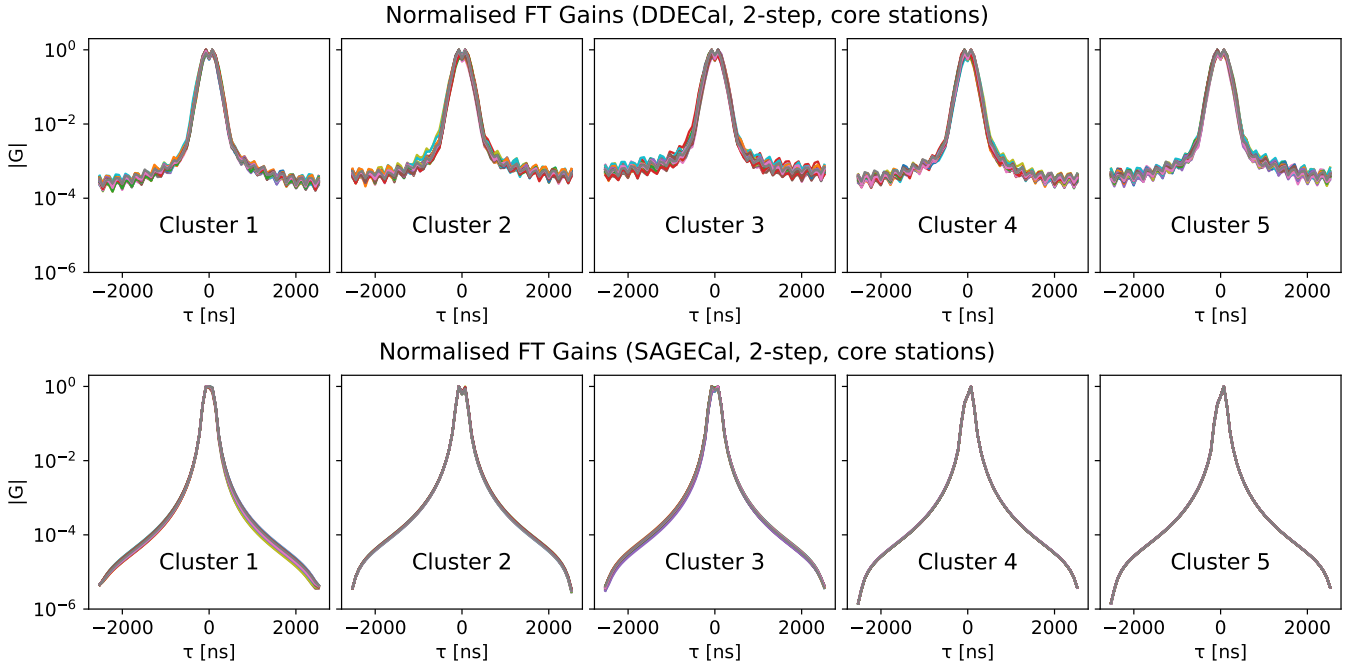


**Fig. 6.** Peak-normalised gain solutions in delay space per station and cluster obtained by DDECAL (on top) and SAGECAL (on bottom) with the 2-step method. Different colours denote solutions for different stations. Each polarisation component is added in quadrature.

**Table 4.** Summary of the GP model for each DD-calibration case.

Hyperparameter	Prior	Estimate			
		DDECAL, 1-step	DDECAL, 2-step	SAGECAL, 1-step	SAGECAL, 2-step
$\eta_{\text{sky}}$	$+\infty$	-	-	-	-
$\sigma_{\text{sky}}^2/\sigma_n^2$	-	355.7	341.5	553.7	502.9
$l_{\text{sky}}$ [MHz]	$\mathcal{U}(10.0, 100.0)^*$	85.67	82.81	41.65	39.08
$\eta_{\text{mix}}$	$3/2$	-	-	-	-
$\sigma_{\text{mix}}^2/\sigma_n^2$	-	43.0	40.9	104.4	97.8
$l_{\text{mix}}$ [MHz]	$\mathcal{U}(0.5, 20.0)$	3.342	3.183	3.697	3.686
$\eta_{\text{ex}}$	$5/2$	-	-	-	-
$\sigma_{\text{ex}}^2/\sigma_n^2$	-	6.5	5.5	7.0	5.9
$l_{\text{ex}}$ [MHz]	$\mathcal{U}(0.2, 0.7)$	0.262	0.253	0.267	0.242
$\eta_{21}$	$1/2$	-	-	-	-
$\sigma_{21}^2/\sigma_n^2$	-	8.44E-04	1.46E-05	1.53E-06	3.21E-07
$l_{21}$ [MHz]	$\mathcal{U}(0.1, 1.2)$	0.806	0.808	0.808	0.810

**Notes.** \* $\mathcal{U}$  indicates a uniform prior.

SAGECAL end up with different residuals in the primary beam after DD-calibration. The sky and mix components are used to model these residuals. Hence it is reasonable to assume that the estimated parameters of the same calibration algorithm converge to similar values for the sky and mix components.

#### 5.4. Power spectra

Fig. 7 shows the resulting cylindrical power spectra after the DD-calibration and foreground removal with four DD-calibration scenarios using DDECAL and SAGECAL. Fig. 8 shows the cylindrical Stokes-I power-spectra ratio after DD-calibration between DDECAL and SAGECAL for the 1-step or 2-step method (top), and the ratio between the 1-step and 2-step calibration method for the fixed DD-calibration algorithm (bottom). On top, red indicates excess power from DDECAL, while blue indicates excess power from SAGECAL. On bottom, red indicates excess power from the 1-step method, and blue from the 2-step method. If the colour is close to white, it means that the ratio between the two methods is close to 1 and the difference is marginal. The dashed lines, from bottom to top, indicate the  $5^\circ$  (the primary beam),  $20^\circ$  and  $90^\circ$  (instrumental horizon) delay lines from the phase centre.

The major difference between DDECAL and SAGECAL is seen in the region of the primary beam (for both 1-step and 2-step methods in Fig. 7 on top and in Fig. 8 on top). We notice that the power in the primary beam region is lower when calibrated by DDECAL. SAGECAL subtracts Cas A and Cyg A better than DDECAL when the 1-step method is used (top left in Fig. 8), however, the difference disappears when the 2-step method is used (top right in Fig. 8). This different performance between the 1-step and 2-step methods with DDECAL is also reflected on the bottom left in Fig. 8. DDECAL with the 1-step method shows significantly higher power between the  $20^\circ$  and  $90^\circ$  delay lines compared to the 2-step method. The difference between the 1-step and 2-step methods is, however, marginal for SAGECAL (bottom right in Fig. 8).

After the GPR foreground removal, which is well suited to remove foreground in the primary beam region, the difference in the primary beam region between DDECAL and SAGECAL is significantly reduced as shown in the bottom row of Fig. 7.

#### 5.5. The North Celestial Pole results

In this subsection, we present the DD-calibration results on the NCP processed by the standard LOFAR-EoR pipeline. The main differences between the DD-calibration examined in this work and the standard pipeline are summarised in Table.5. The NCP sky images after DI- and DD-calibration can be found in Appendix.D.

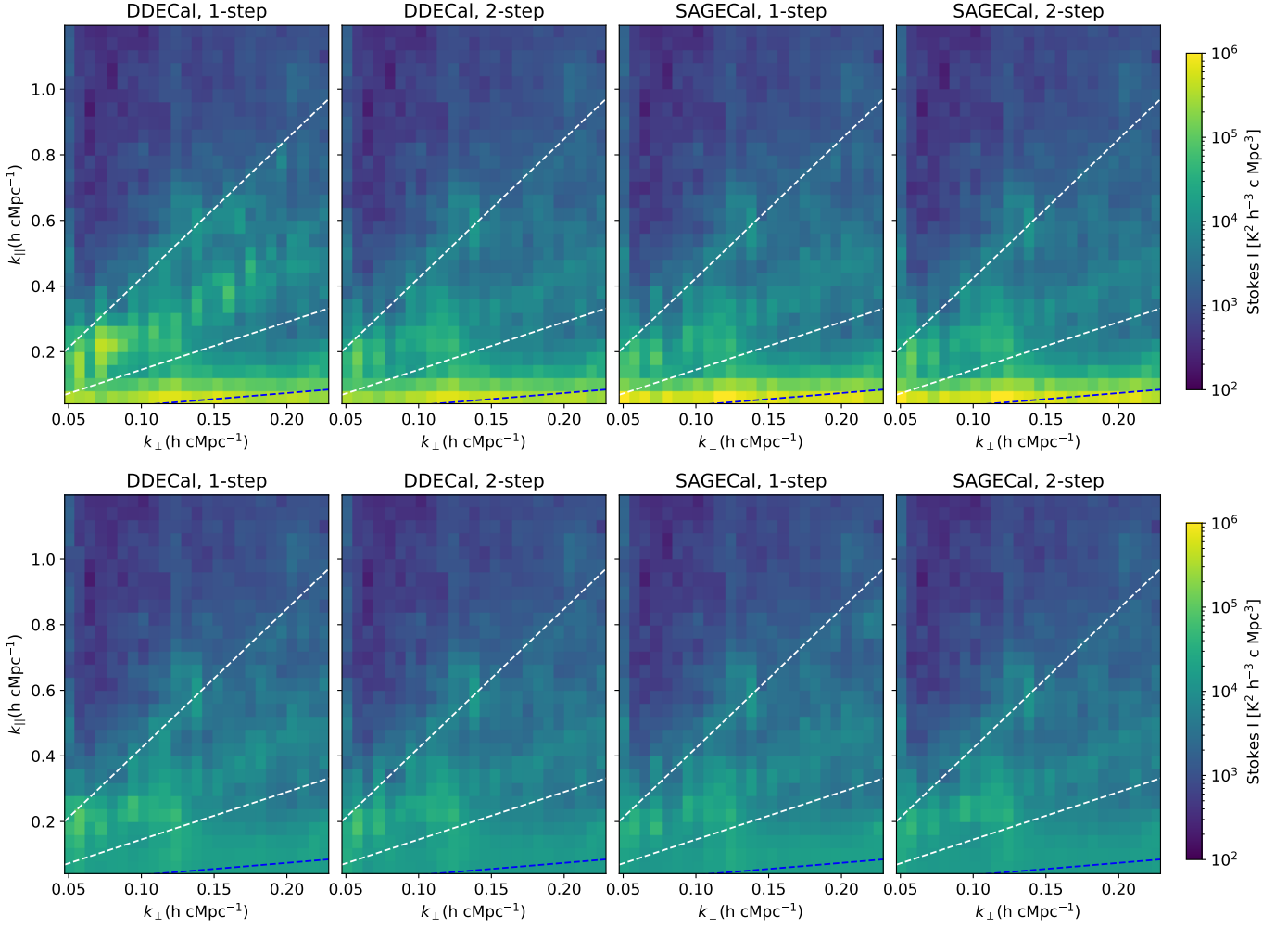
##### 5.5.1. Images

Fig. 9 shows the full sky Stokes-I residual images on the NCP after the DI (top left) and DD-calibration (top right). The residual images after DI- and DD-calibration (with SAGECAL and 2-step method) are shown on bottom for comparison. Most sources show significantly reduced power after the DD-calibration on the NCP, however, we still see the imprint of Cas A and Cyg A in the residuals.

Compared to the residuals of the RA 18h flanking field in Fig. 5 (bottom right), the residual power around the phase centre is significantly lower on the NCP, due to the application of the extensive sky model and more directions during the DD-calibration in the NCP processing.

However, the subtraction of Cas A and Cyg A does not show better performance on the NCP compared to the RA 18h flanking field. While the residuals of Cas A are slightly more compact on the NCP than the RA 18h flanking field, the residuals of Cyg A have significantly lower power on the RA 18h flanking field.

In Table.6, the calibration setup details for the Cas A and Cyg A subtraction on the NCP with the standard processing and flanking field with the best results using SAGECAL and the 1-step method are summarised. In both cases, the calibration is carried out by SAGECAL using the shapelet model. One main difference is the time interval of solutions in the two fields. The NCP uses a higher resolution, one solution per 2.5 min, compared to the 10-min interval of the RA 18h flanking field in this particular case. This also indicates that solving gains for a finer time interval does not always improve the calibration performance, because it is more likely to overfit the data and increase noise. Hence, finding an optimal calibration setup is crucial for the calibration performance, given a calibration algorithm and a sky model.



**Fig. 7.** Cylindrical Stokes-I power spectra after DD-calibration (top) and GPR foreground removal (bottom) with four DD-calibration scenarios using DDECAL and SAGECAL. The dashed lines, from bottom to top, correspond to the  $5^\circ$  (the primary beam),  $20^\circ$  and  $90^\circ$  (instrumental horizon) delay lines from the phase centre. From the top row to the bottom row, the GPR foreground removal technique efficiently removes the residual power in the primary beam region. As we noted in the residual images in Fig. 4 (middle and bottom), SAGECAL (last two panels on top) leaves slightly higher power in the primary beam region than DDECAL (first two panels on top) after DD-calibration. However, this difference in the primary beam disappears after the application of GPR (bottom). Also, the power spectrum of DDECAL and 1-step method before GPR (first panel on top) has higher residual power between  $20^\circ$  and  $90^\circ$  delay lines compared to the rest, which indicates poor subtraction of Cas A and Cyg A. However, after GPR, the residual Stokes-I power spectra from the four different DD-calibration scenarios show very similar results.

**Table 5.** Main differences between the DD-calibrations used in this work and in the standard LOFAR-EoR pipeline.

Parameter	NCP	RA 18h flanking field
Number of components	$\sim 28000$	3389*
Number of clusters	122	20*
Baselines	50 – 250 $\lambda$	
Solution time interval	2.5 – 20 min**	10 min
Solution frequency interval	per sub-band (195.3 kHz)	

**Notes.** \*Without Cas A and Cyg A. \*\*Gain solution time interval varies, depending on the cluster in the NCP analysis.

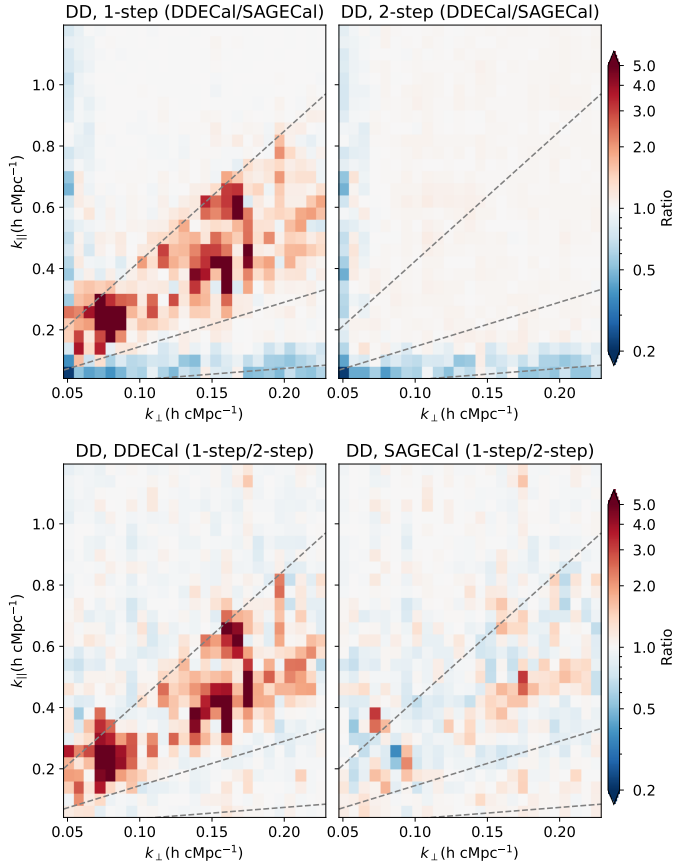
### 5.5.2. Power spectra

Fig. 10 shows the cylindrical Stokes-I power spectra after the DD-calibration and GPR foreground removal on the NCP. A few  $k_\perp$  modes are flagged, due to bad data quality. Compared to the cylindrical Stokes-I residual power spectra of the RA 18h flanking field in Fig. 7 on bottom, the NCP has higher power on short

baselines ( $k_\perp \sim 0.05 - 0.13 \text{ h-cMpc}^{-1}$ ), in particular, between the  $20^\circ$  and  $90^\circ$  delay lines and around the  $90^\circ$  delay line.

Fig. 11 shows the ratio of cylindrical Stokes-I power spectra between the flanking field and NCP field after DD-calibration (top) and after GPR foreground removal (bottom). Red indicates excess power from the flanking field and blue indicates excess





**Fig. 8.** Cylindrical Stokes-I power spectra ratio after DD-calibration between DDECAL and SAGECAL given a calibration strategy, the 1-step or 2-step method (on top), and between the 1-step and 2-step methods given a DD-calibration algorithm, DDECAL or SAGECAL (on bottom). The dashed lines indicate the  $5^\circ$  (the primary beam),  $20^\circ$  and  $90^\circ$  (instrumental horizon) delay lines from the phase centre from bottom to top. On top, red indicates excess power from DDECAL and blue indicates excess power from SAGECAL. On bottom, red indicates excess power from the 1-step method and blue indicates excess power from the 2-step method.

**Table 6.** Comparison of the Cas A and Cyg A subtraction setup of the NCP in the standard processing with SAGECAL and the RA 18h flanking field with SAGECAL and the 1-step method.

Parameter	NCP	RA 18h flanking field
Calibration algorithm	SAGECAL	
Model	Shapelet model	
Number of clusters	2	
Solution time interval	2.5 min	10 min
Solution frequency interval	per sub-band (195.3 kHz)	

power from the NCP field. Again, a few  $k_\perp$  modes are flagged, due to bad data quality after GPR foreground removal (bottom). As we have noticed before, the flanking field has higher residual power in the foreground region (below the  $20^\circ$  delay line) after DD-calibration on top. This power is stronger with SAGECAL (last two panels on top) than with DDECAL (first two panels on top). However, after GPR foreground removal, the excess power is well removed (bottom). Finally, the major difference comes from the excess power from the NCP on short baselines ( $k_\perp \sim 0.05 - 0.13 \text{ h-cMpc}^{-1}$ ) around the  $90^\circ$  delay line as we have already seen in Fig. 10.

It is unclear where this extra power is from. Because the data on the two fields are from the same observing run only with the station beams and array phased up differently, they are supposed to have similar RFI and systematics. The NCP has a known disadvantage that stationary RFI sources can add coherently via its side-lobes. We, therefore, perform an extra RFI flagging step after DD-calibration to mitigate this effect on the NCP. However, this extra flagging step does not show a significant improvement.

### 5.6. Spherically-averaged power spectra and upper limits

Fig. 12 shows the spherically-averaged Stokes-I power spectra of the RA 18h flanking field with four different DD-calibration scenarios and the NCP at different stages of the processing, the DI-calibration, DD-calibration and foreground removal (in green, red and blue). After the DI-calibration, the Stokes-I power is higher in the RA 18h flanking field than in the NCP, however, this tendency reverses after the DD-calibration (up to  $k \sim 0.7 \text{ h} \cdot \text{cMpc}^{-1}$ ), as we discussed earlier, likely due to the extensive sky model and clustering used for the DD-calibration on the NCP. However, this advantage disappears once we apply the GPR foreground removal technique. The Stokes-I power of the RA 18h flanking field is lower than that of the NCP by a factor of 1.2 – 2 over  $k = 0.075 - 0.6 \text{ h-cMpc}^{-1}$ .

We also compare the  $2\text{-}\sigma$  upper limits of the 21-cm signal on the RA 18h flanking field and NCP (in Table.7). Compared to the NCP results, the RA 18h flanking field shows around 10 – 30% improved upper limits over all  $k$  values considered for the four different calibration scenarios.

The  $2\text{-}\sigma$  upper limits on the 21-cm signal after the calibration and foreground removal by the four different DD-calibration scenarios are summarised in Table.7. The 2-step SAGECAL method presents the best upper limit results compared to others. Within the four cases studied, SAGECAL provides 5 – 10% better upper limits compared to DDECAL given a calibration strategy, 1-step or 2-step. The 2-step method produces 3 – 8% better upper limits given a calibration algorithm, DDECAL or SAGECAL. This difference is minor and could also come from the different model assumptions (e.g. between apparent and intrinsic flux models, and/or between different Cas A and Cyg A models), apart from the difference in the model clustering and the application of the primary beam model.

## 6. Conclusions

In this work, we have compared the performance of two DD-calibration algorithms, DDECAL and SAGECAL, in the context of LOFAR-EoR 21-cm power spectra by processing a single observation night on a flanking field of the North Celestial Pole (NCP) obtained by Low Frequency Array (LOFAR). We applied two different strategies for subtracting the very bright sources Cas A and Cyg A, predicting and subtracting the two sources simultaneously with the sky model, namely, the 1-step method, or in a separate step before predicting and subtracting the sky model, the 2-step method. We conclude the following:

(1) We do notice that there are differences between the two DD-calibration algorithms. DDECAL shows a better performance in subtracting sources in the primary beam region, probably due to the application of the beam model during the DD-calibration. This suggests that having a beam model during the DD-calibration significantly improves the calibration performance, especially, in the primary beam region.

(2) SAGECAL, on the other hand, shows a better performance in subtracting Cas A and Cyg A. While predicting and subtract-

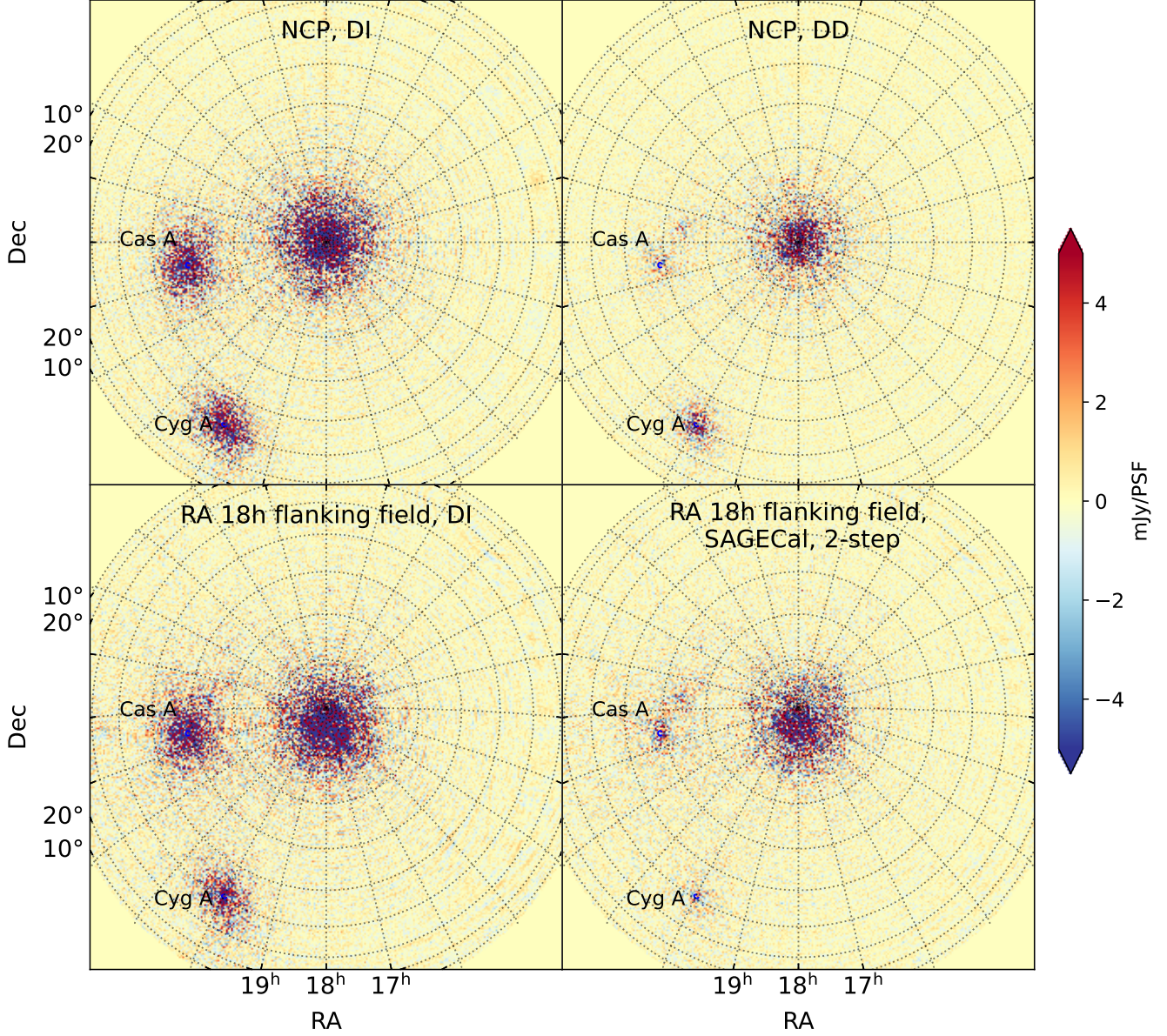


**Fig. 9.** Comparison of full sky ( $120^\circ \times 120^\circ$ ) Stokes-I residual images created by using 69 sub-bands and  $50 - 300\lambda$  baseline cut and integrating the full observation after DI (first column) and DD-calibration (second column) on the NCP (top) and on the RA 18h flanking field (bottom). The DD-calibration is performed by SAGECAL with an extensive sky model ( $\sim 28000$  sources) on the NCP and with a simpler sky model ( $\sim 3400$  sources) on the RA 18h flanking field. The residual power around the centre is substantially lower on the NCP (top right) than the flanking field (bottom right), due to using an extensive sky model with more directions during the DD-calibration. The power from Cas A and Cyg A is significantly reduced after DD-calibration. The residuals of Cas A are stronger on the NCP (top right) than on the flanking field (bottom right). Unphysical sources below the horizon are masked.

ing Cas A and Cyg A in a separate step does not change the DD-calibration results significantly for SAGECAL, it does make a significant difference for DDECAL. The time and frequency smearing correction is applied for SAGECAL but not for DDECAL in this work. The difference in subtracting Cas A and Cyg A could be due to the application of this smearing correction.

(3) The difference of the residual power in the primary beam region between DDECAL and SAGECAL becomes marginal when the GPR foreground removal is applied after DD-calibration.

(4) We also compare the results on the RA 18h flanking field with the NCP results processed by the standard LOFAR-EoR pipeline. The standard processing pipeline uses a very extended

sky model (with  $\sim 28000$  sources) and 122 directions for the DD-calibration which makes the processing computationally expensive.

(5) For the four different DD-calibration scenarios studied, comparable upper limits on the 21-cm power spectra on the NCP flanking field are achieved, using a simpler sky model (with  $\sim 3500$  sources including Cas A and Cyg A) and fewer directions (20 directions), when the foreground removal technique, Gaussian Process Regression (GPR), is used after DD-calibration.

(6) In both NCP and RA 18h flanking field results, even after DD-calibration, Cas A and Cyg A are the most dominant sources



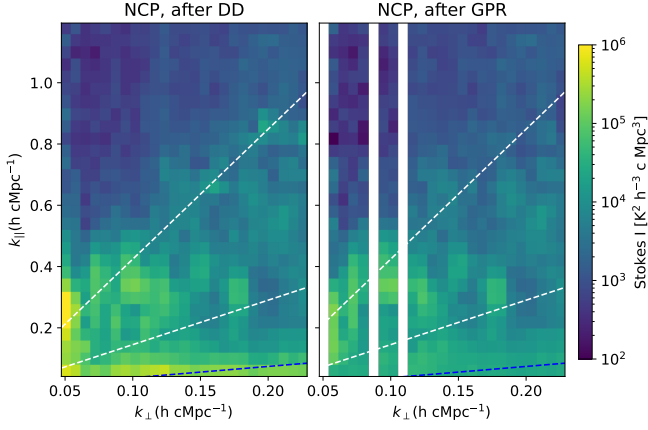


**Fig. 10.** Cylindrical Stokes-I power spectra after DD-calibration (left) processed by the standard LOFAR-EoR pipeline with SAGECAL and GPR foreground removal (right) of a single observation night on the NCP. The dashed lines indicate the 5° (the primary beam), 20° and 90° (instrumental horizon) delay lines from the phase centre from bottom to top, respectively. Some bad quality data are flagged on right.

of residuals in the far field in full sky images in Fig. 9 and 5, which agrees with the previous study on sources of excess variance in the LOFAR-EoR 21-cm power spectra (Gan et al. 2022). They may be contributors to the excess noise in the wedge.

Based on our analysis, we suggest the following strategies for future improvements:

**Apply time and frequency smearing corrections for DDECAL:** the latest version of DDECAL corrects for the time and frequency smearing. This correction is not applied during the DD-calibration process in this work. In future, we would like to include the smearing correction during the DD-calibration and investigate whether it further improves the calibration performance, especially the subtraction of Cas A and Cyg A.

**Apply a beam model for SAGECAL:** the future versions of SAGECAL will support the LOFAR beam model. Our results with DDECAL show that applying a beam model is likely to improve the source subtraction around the phase centre substantially. We expect to achieve similar source subtraction performance with SAGECAL, once we apply a beam model for SAGECAL.

**Process flanking fields for cross-checks:** in this work, we have processed a single observation night on two different fields, the NCP and one of its flanking fields, using different calibration setups and compared their results. While the data sets from the same observation share the same or very similar RFI, ionosphere and systematics, we note that the residuals in the two fields look rather different than expected. In particular, the NCP shows extra power above the wedge on short baselines that is not present in the RA 18h flanking field. We suspect that this power partially comes from the residuals of Cas A and Cyg A, however, more investigations are needed to clarify the source(s) of the extra power. By processing other flanking fields of the same observation and imaging ground planes, we will be able to identify whether this is a particular problem of the NCP field that is related to the beam or a calibration issue.

**Optimise DD-calibration parameters:** by comparing the performance of the four different DD-calibration scenarios, even with the same sky model, depending on the calibration parameters and strategies we use, such as frequency smoothing constraints or the number of clusters for particularly bright sources, the calibration outcome can be significantly different. While there are some studies on the regularisation of frequency in

**Table 7.**  $2\text{-}\sigma$  upper limit of the 21-cm signal  $\Delta_{21}^2$  from a single observation night on the RA 18h flanking field with different DD-calibration scenarios and the NCP calibrated by the standard pipeline with SAGECAL.

DDECAL, 1-step		DDECAL, 2-step	
$k$ [h·cMpc <sup>-1</sup> ]	$\Delta_{21}^2$ [mK <sup>2</sup> ]	$k$ [h·cMpc <sup>-1</sup> ]	$\Delta_{21}^2$ [mK <sup>2</sup> ]
0.0764	(766) <sup>2</sup>	0.0760	(736) <sup>2</sup>
0.1055	(1154) <sup>2</sup>	0.1054	(1067) <sup>2</sup>
0.1454	(1874) <sup>2</sup>	0.1454	(1721) <sup>2</sup>
0.2002	(3102) <sup>2</sup>	0.2002	(2817) <sup>2</sup>
0.2699	(3755) <sup>2</sup>	0.2699	(3487) <sup>2</sup>
0.3756	(3968) <sup>2</sup>	0.3755	(3843) <sup>2</sup>
0.5184	(5299) <sup>2</sup>	0.5183	(4771) <sup>2</sup>

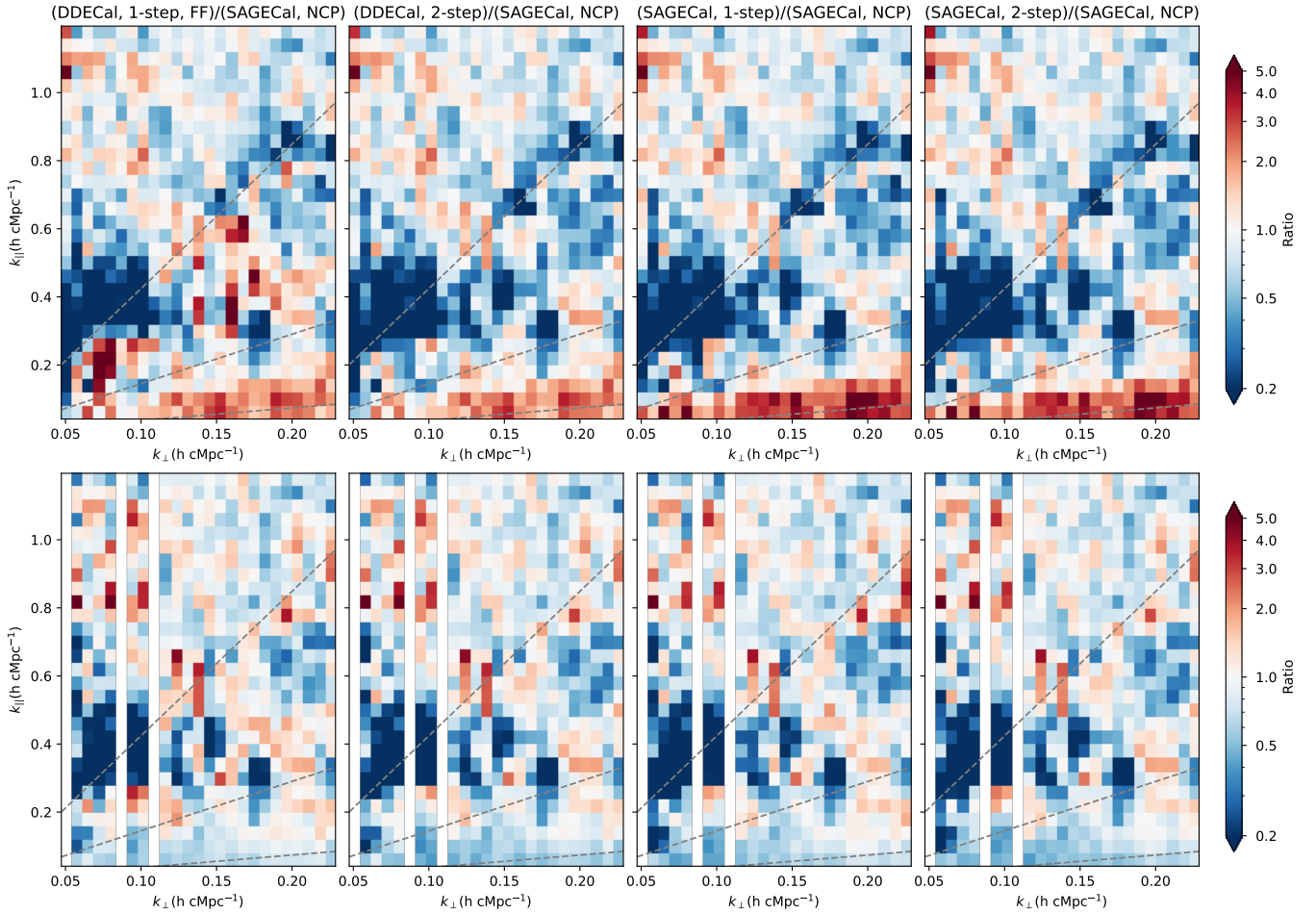
SAGECAL, 1-step		SAGECAL, 2-step	
$k$ [h·cMpc <sup>-1</sup> ]	$\Delta_{21}^2$ [mK <sup>2</sup> ]	$k$ [h·cMpc <sup>-1</sup> ]	$\Delta_{21}^2$ [mK <sup>2</sup> ]
0.0759	(678) <sup>2</sup>	0.0759	(666) <sup>2</sup>
0.1054	(1021) <sup>2</sup>	0.1053	(1007) <sup>2</sup>
0.1452	(1725) <sup>2</sup>	0.1453	(1636) <sup>2</sup>
0.1999	(2839) <sup>2</sup>	0.2000	(2660) <sup>2</sup>
0.2700	(3380) <sup>2</sup>	0.2699	(3395) <sup>2</sup>
0.3755	(3854) <sup>2</sup>	0.3755	(3688) <sup>2</sup>
0.5182	(4892) <sup>2</sup>	0.5181	(4605) <sup>2</sup>

NCP, standard	
$k$ [h·cMpc <sup>-1</sup> ]	$\Delta_{21}^2$ [mK <sup>2</sup> ]
0.0781	(1041) <sup>2</sup>
0.1047	(1608) <sup>2</sup>
0.1471	(2457) <sup>2</sup>
0.2016	(3167) <sup>2</sup>
0.2685	(4041) <sup>2</sup>
0.3740	(6508) <sup>2</sup>
0.5168	(5896) <sup>2</sup>

the DD-calibration (Yatawatta 2015, 2016; Mevius et al. 2022), more studies are needed, in particular, for the selection of the number of clusters and solution intervals. Different calibration parameters can be tested relatively straightforward because it does not require modifying the existing sky model or pipeline.

*Acknowledgements.* HG and LVEK would like to acknowledge support from the Centre for Data Science and Systems Complexity (DSSC) at the University of Groningen and a Marie Skłodowska-Curie COFUND grant, no.754315. BKG and LVEK acknowledge the financial support from the European Research Council (ERC) under the European Union's Horizon 2020 research and innovation programme (Grant agreement No. 884760, "CoDEX").



**Fig. 11.** Cylindrical Stokes-I power spectra ratio after DD-calibration (top) and GPR foreground removal (bottom) between the flanking field and the NCP field. The dashed lines, from bottom to top, correspond to the 5° (the primary beam), 20° and 90° (instrumental horizon) delay lines from the phase centre. Red indicates excess power from the flanking field and blue indicates excess power from the NCP field. Some bad data are flagged on bottom. From top to bottom, the residual foregrounds below the 20° delay line (i.e. excess power from the flanking field) are well removed after GPR foreground removal.

## Data Availability

The data underlying this article will be shared upon request to the corresponding author.

## References

- Arras, P., Frank, P., Leike, R. H., Westermann, R., & Ensslin, T. A. 2019, *A & A*, 618, 100
- Baldwin, J. E., Boysen, R. C., Hales, S. E. G., et al. 1985, *MNRAS*, 217, 717
- Barry, N., Hazelton, B., Sullivan, I., Morales, M. F., & Pober, J. C. 2016, *MNRAS*, 461, 3135–3144
- Barry, N., Wilensky, M., Trott, C. M., et al. 2019b, *ApJ*, 884, 1
- Bernardi, G., de Bruyn, A. G., Harker, G., et al. 2010, *A&A*, 522, A67
- Born, M., Wolf, E., Bhatia, A. B., et al. 1999, *Principles of Optics: Electromagnetic Theory of Propagation, Interference and Diffraction of Light*, 7th edn. (Cambridge University Press)
- Bowman, J. D., Cairns, I., Kaplan, D. L., et al. 2013, *PASA*, 30, e031
- Bowman, J. D., Morales, M. F., & Hewitt, J. N. 2009, *ApJ*, 695, 183
- Bowman, J. D., Rogers, A. E. E., Monsalve, R. A., Mozden, T. J., & Mahesh, N. 2018, *Nature*, 555, 67–70
- Boyd, S., Parikh, N., Chu, E., Peleato, B., & Eckstein, J. 2011, *Foundations and Trends in Machine Learning*, 3, 1
- Cheng, C., Parsons, A. R., Kolopanis, M., et al. 2018, *ApJ*, 868, 26
- Cornwell, T. J. & Wilkinson, P. N. 1981, *MNRAS*, 196, 1067
- DeBoer, D. R., Parsons, A. R., Aguirre, J. E., et al. 2017, *PASP*, 129, 045001
- Edler, H. W., de Gasparin, F., & Rafferty, D. 2021, *A&A*, 652, A37
- Farouki, R. & Rajan, V. 1988, *Computer Aided Geometric Design*, 5, 1
- Fessler, J. & Hero, A. 1994, *IEEE Transactions on Signal Processing*, 42, 2664
- Furlanetto, S. R., Peng Oh, S., & Briggs, F. H. 2006, *Physics Reports*, 433, 181
- Gan, H., E Koopmans, L. V., Mertens, F. G., et al. 2022, *arXiv e-prints*, arXiv:2203.02345
- Gehlot, B. K., Mertens, F. G., Koopmans, L. V. E., et al. 2019, *MNRAS*, 488, 4271
- Greenhill, L. J. & Bernardi, G. 2012, *HI Epoch of Reionization Arrays*
- Hamaker, J. P., Bregman, J. D., & Sault, R. J. 1996, *A&AS*, 117, 137
- HERA Collaboration, Abdurashidova, Z., Aguirre, J., et al. 2021, *astro-ph.CO* [arXiv:2108.07282]
- Kazemi, S. & Yatawatta, S. 2013, *MNRAS*, 435, 597
- Kazemi, S., Yatawatta, S., Zaroubi, S., et al. 2011, *MNRAS*, 414, 1656
- Kolopanis, M., Jacobs, D. C., Cheng, C., et al. 2019, *ApJ*, 883, 133
- Koopmans, L. V. E., Pritchard, J., Mellema, G., et al. 2015, *The Cosmic Dawn and Epoch of Reionization with the Square Kilometre Array*
- Li, W., Pober, J. C., Barry, N., et al. 2019, *ApJ*, 887, 141
- Liu, A. & Shaw, J. R. 2020, *Publications of the Astronomical Society of the Pacific*, 132, 062001
- Liu, D. & Nocedal, J. 1989, *Mathematical Programming* 45, 503–528
- McQuinn, M., Zahn, O., Zaldarriaga, M., Hernquist, L., & Furlanetto, S. R. 2006, *ApJ*, 653, 815
- Mellema, G., Koopmans, L. V. E., Abdalla, F. A., et al. 2013, *Experimental Astronomy*, 36, 235
- Mertens, F. G., Ghosh, A., & Koopmans, L. V. E. 2018, *MNRAS*, 478, 3640
- Mertens, F. G., Mevius, M., Koopmans, L. V. E., et al. 2020, *MNRAS*, 493, 1662
- Mevius, M., Mertens, F., Koopmans, L. V. E., et al. 2022, *MNRAS*, 509, 3693
- Mevius, M., van der Tol, S., Pandey, V. N., et al. 2016, *Radio Science*, 51, 927–941
- Mitchell, D., Greenhill, L., Wayth, R., et al. 2008, *Selected Topics in Sig. Proc., IEEE Journal of*, 2, 707
- Morales, M. F. & Hewitt, J. 2004, *ApJ*, 615, 7

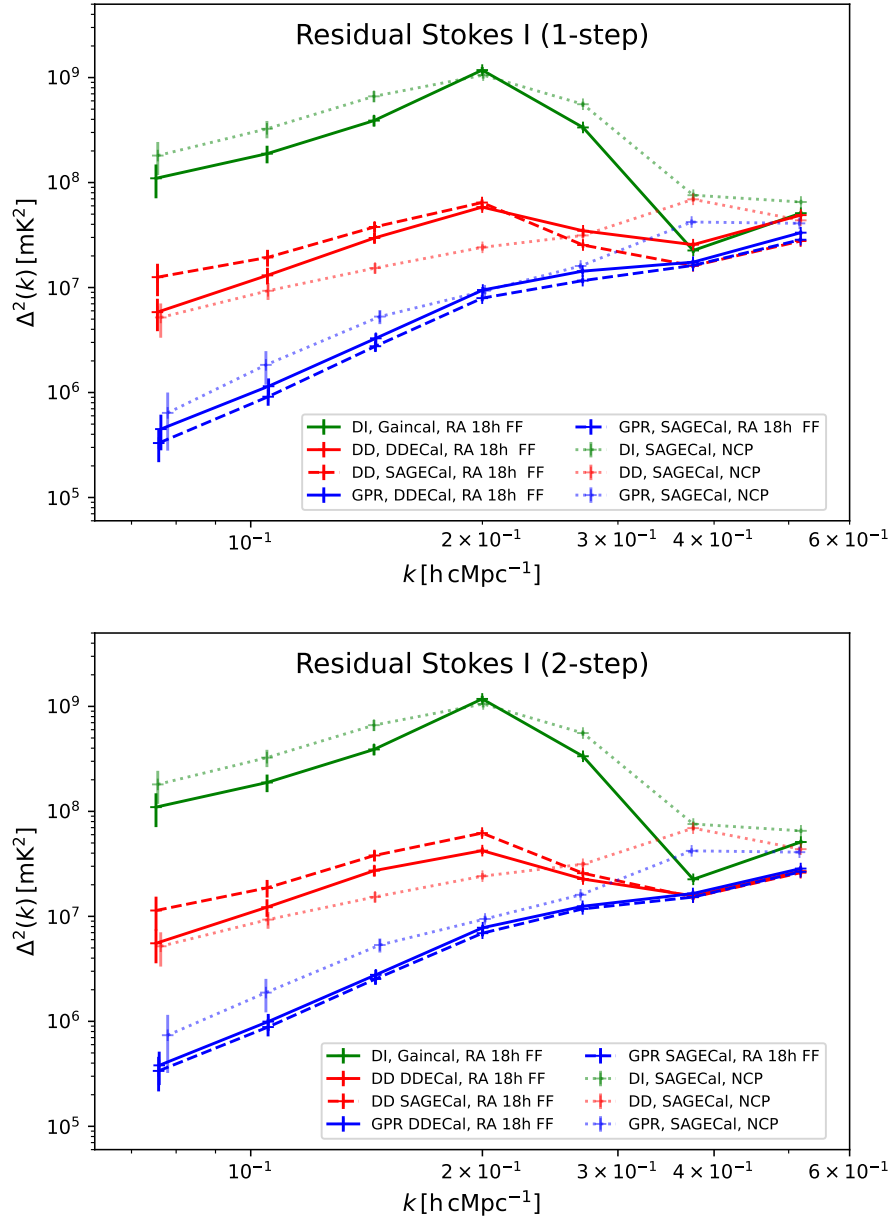


**Fig. 12.** Spherically-averaged Stokes-I power spectra on the NCP calibrated by the standard LOFAR-EoR pipeline with SAGECAL (dotted lines) and the RA 18h flanking field calibrated by DDECAL (solid lines) or SAGECAL (dashed lines) with the 1-step (on top) or 2-step (on bottom) method. Colours denote different processing stages. Green, red and blue denote the Stokes-I power spectra after DI-calibration, DD-calibration and GPR foreground removal, respectively. After each calibration stage, the Stokes-I power is reduced significantly. The NCP results show lower power after DD-calibration at low  $k$  ( $< 0.3 \text{ h} \cdot \text{cMpc}^{-1}$ ) compared to the RA 18h flanking field (in red), due to using an extensive sky model, however, after the GPR foreground removal, the RA 18h flanking field has lower power compared to the NCP (in blue). DDECAL (solid lines) shows better subtraction of sources after DD-calibration (in red) compared to SAGECAL (dashed lines) in both 1-step and 2-step methods, due to the application of the beam model, however, this advantage disappears after GPR (in blue).

Morales, M. F. & Wyithe, J. S. B. 2010, *Annual Review of Astronomy and Astrophysics*, 48, 127  
Mouri Sardarabadi, A. & Koopmans, L. V. E. 2018, *MNRAS*, 483, 5480  
Noordam, J. & Oschmann, J. 2004, *Proc. SPIE Conf. Ser. Vol. 5489, Ground-based Telescopes*  
Offringa, A. R., de Bruyn, A. G., Zaroubi, S., et al. 2013, *A&A*, 549, A11  
Offringa, A. R., McKinley, B., Hurley-Walker, N., et al. 2014, *MNRAS*, 444, 606  
Offringa, A. R., Mertens, F., & Koopmans, L. V. E. 2019a, *MNRAS*, 484, 2866  
Offringa, A. R., Mertens, F., van der Tol, S., et al. 2019b, *A&A*, 631, A12  
Offringa, A. R. & Smirnov, O. 2017, *MNRAS*, 471, 301  
Offringa, A. R., Trott, C. M., Hurley-Walker, N., Johnston-Hollitt, M., et al. 2016, *MNRAS*, 458, 1057  
Offringa, A. R., van de Gronde, J. J., & Roerdink, J. B. T. M. 2012, *A&A*, 539

Ollier, V., El Korso, M. N., Ferrari, A., Boyer, R., & Larzabal, P. 2018, *Signal Processing*, 153, 348  
Paciga, G., Albert, J. G., Bandura, K., et al. 2013, *MNRAS*, 433, 639  
Paciga, G., Chang, T.-C., Gupta, Y., et al. 2011, *MNRAS*, 413, 1174  
Pandey, V., Koopmans, L., Tiesinga, E., et al. 2020, *ADASS XXIX. ASP Conference Series*, 524  
Parsons, A. R., Poher, J. C., Aguirre, J. E., et al. 2012, *ApJ*, 756, 165  
Patil, A. H., Yatawatta, S., Koopmans, L. V. E., et al. 2017, *ApJ*, 838, 65  
Patil, A. H., Yatawatta, S., Zaroubi, S., et al. 2016, *MNRAS*, 463, 4317  
Pearson, T. J. & Readhead, A. C. S. 1984, *ARA&A*, 22, 97  
Philip, L., Abdurashidova, Z., Chiang, H., et al. 2018, *Journal of Astronomical Instrumentation*, 08  
Pritchard, J. R. & Loeb, A. 2012, *Reports on Progress in Physics*, 75, 086901  
Rasmussen, C. E. & Williams, C. K. I. 2005, *Gaussian Processes for Machine Learning* (The MIT Press)

- Salvini, S. & Wijnholds, S. J. 2014, in 2014 XXXIth URSI General Assembly and Scientific Symposium (URSI GASS), 1–4
- Singh, S., Subrahmanyan, R., Shankar, N. U., et al. 2017, *AJ*, 845, L12
- Smirnov, O. M. 2011, *A&A*, 527, A106
- Smirnov, O. M. & Tasse, C. 2015, *MNRAS*, 449, 2668
- Tasse, C. 2014, *A&A*, 566, A127
- Thekkepattu, J. N., Subrahmanyan, R., Somashekar, R., et al. 2021, *Experimental Astronomy*
- van Diepen, G., Dijkema, T. J., & Offringa, A. 2018, *DPPP: Default Pre-Processing Pipeline*
- van Haarlem, M. P., Wise, M. W., Gunst, A. W., et al. 2013, *A&A*, 556, A2
- Vedantham, H. K. & Koopmans, L. V. E. 2016, *MNRAS*, 458, 3099
- Yatawatta, S. 2011, *URSI General Assembly and Scientific Symposium*, 1
- Yatawatta, S. 2015, *MNRAS*, 449, 4506
- Yatawatta, S. 2016, *Fine tuning consensus optimization for distributed radio interferometric calibration*
- Yatawatta, S. 2019, *MNRAS*, 486, 5646
- Yatawatta, S., Clercq, L. D., Spreeuw, H., & Diblen, F. 2019, *IEEE Data Science Workshop (DSW)*, 208
- Yatawatta, S., de Bruyn, A. G., Brentjens, M. A., et al. 2013, *A&A*, 550, A136
- Zheng, Q., Wu, X.-P., Johnston-Hollitt, M., Gu, J.-h., & Xu, H. 2016, *ApJ*, 832, 190

- 
- <sup>1</sup> Kapteyn Astronomical Institute, University of Groningen, PO Box 800, 9700AV Groningen, The Netherlands  
e-mail: hgan@astro.rug.nl
- <sup>2</sup> LERMA (Laboratoire d’Etudes du Rayonnement et de la Matière en Astrophysique et Atmosphères), Observatoire de Paris, PSL Research University, CNRS, Sorbonne Université, F-75014 Paris, France
- <sup>3</sup> The Netherlands Institute for Radio Astronomy (ASTRON), PO Box 2, 7990AA Dwingeloo, The Netherlands
- <sup>4</sup> Max-Planck Institute for Astrophysics, Karl-Schwarzschild-Straße 1, D-85748 Garching, Germany
- <sup>5</sup> School of Earth and Space Exploration, Arizona State University, Tempe, Az 85281, USA
- <sup>6</sup> Astrophysics Research Center (ARCO), Department of Natural Sciences, The Open University of Israel,  
1 University Road, PO Box 808, Ra’anana 4353701, Israel
- <sup>7</sup> Department of Physics, Technion, Haifa 32000, Israel
- <sup>8</sup> Institute for Computational Science, University of Zurich, Winterthurerstraße 190, CH-8057 Zurich, Switzerland
- <sup>9</sup> Astronomy Centre, Department of Physics and Astronomy, University of Sussex, Pevensey II Building, Brighton BN1 9QH, UK

## Appendix A: NCP flanking field configuration

In Table A.1, the pointing and beam number of the NCP and six flanking fields are summarised. The phase centres of the six flanking fields are located  $4^\circ$  from the NCP field. In this work, we focus on the RA 18h field.

## Appendix B: Sky model details

Here we provide detailed information about the sky model on the RA 18h flanking field. The flux of the model is scaled using four calibrators summarised in Table. B.1. The details of sky model clustering are summarised in Table. B.2.

## Appendix C: Difference images of DD-calibration residuals

In Fig. C.1, we show the difference in residuals after different calibration scenarios. The Stokes-I residual images after DD-calibration with the four scenarios in Fig. 4 are respectively subtracted by the residual image of the DDECAL and 1-step method (middle left in Fig. 4).

In Fig. C.1, red indicates under-subtraction and blue indicates over-subtraction of sources, compared to the DD-calibration scenario with DDECAL and 1-step method. We use the same reference source (marked with a dashed blue circle) to compare residuals after DD-calibration. Residuals of the source appear lightly blue (indicating marginal over-subtraction) in the DDECAL and 2-step method scenario (bottom left) while residuals appear red in the two SAGECAL scenarios (top and bottom right), indicating under-subtraction.

Overall, DDECAL with the 2-step method shows under-subtraction with most sources appearing red and relatively compact. SAGECAL shows rather scattered residuals with a mixture of over-subtraction and under-subtraction for sources. The difference between the 1-step and 2-step methods is rather small for SAGECAL.

## Appendix D: NCP sky images after DI- and DD-calibration

In Fig. D.1, we present the  $20^\circ \times 20^\circ$  and zoomed ( $4^\circ \times 4^\circ$ ) images on the NCP after DI-calibration (on top) and after DD-calibration (on bottom). Compared to the RA 18h flanking field results in Fig. 4, the NCP shows better subtraction of the foregrounds in the primary beam region, these are likely due to the application of an extended sky model ( $\sim 8$  times more components compared to the RA 18h flanking field sky model) and more directions ( $\sim 6$  times more directions compared to the RA 18h flanking field) during the DD-calibration. The downside is that using an extended sky model and solving gains for more direction can be computationally much more expensive (the NCP standard processing time is  $\sim 5$  times longer compared to the flanking field processing time, in this work). In this work, we note that power spectra similar to the ones obtained by the NCP processing can be achieved with a relatively simple sky model and fewer directions during the DD-calibration, if the GPR foreground removal technique is applied.

## Appendix E: Gain dynamic spectra

Here, we present the gain spectra of one station (CS001HBA0) per cluster obtained with the 1-step (on top) and 2-step (on bottom), achieved by the calibration algorithm, either DDECAL (in

Fig. E.1) or SAGECAL (Fig. E.2). From each figure, by comparing the gain spectra between the 1-step and 2-step methods, we can find how the subtraction of Cas A and Cyg A impacts the gains of the remaining sources in the phase centre.

Depending on the flux type of the sky model used for the calibration, obtained gains show distinct values. DDECAL uses an intrinsic sky model and SAGECAL uses an apparent model, average gain values are higher for SAGECAL than DDECAL. The gain spectra of DDECAL are also flatter than SAGECAL, due to the application of the beam model.

To investigate the difference between the 1-step and 2-step methods, we create gain ratio spectra between the two methods given a calibration algorithm in Fig. E.3 for CS001HBA0 per cluster. We find that the gain difference between the 1-step and 2-step methods is rather big in SAGECAL than in DDECAL. While this difference is more concentrated in the clusters close to the phase centre for DDECAL, from cluster 2 to 7, the difference is more obvious in outer clusters, from cluster 11 to 20, for SAGECAL.

We also present the Cas A and Cyg A gain spectra from different calibration setups in Fig. E.4. First, we compare the gain spectra obtained by the 1-step method using DDECAL (in the first row) and SAGECAL (in the second row). The solution interval is 10 min for both cases. The gains vary more rapidly over time for DDECAL, in this case, and gains from SAGECAL are rather flat. In particular, the gains from SAGECAL are smoother in frequency, compared to DDECAL. This improved smoothness in frequency of SAGECAL possibly contributed to the better performance of the subtraction of Cas A and Cyg A in Fig. 5.

In the last row of Fig. E.4, we present the Cas A and Cyg A gain spectra obtained by DDECAL and the 2-step method. The solutions have a higher resolution, i.e., a 5 min interval, and the gain spectra have more structures in time, compared to the lower resolution solutions in the first two rows. While SAGECAL with the 1-step method (in the second row) and DDECAL with the 2-step method (in the last row) show comparable performance in subtracting Cas A and Cyg A, it is yet unclear whether the added structures in the gain spectra obtained by DDECAL and the 2-step method are physical or noise. And more studies are needed to find out optimal frequency constraints and solution time intervals for calibration.

**Table A.1.** Summary of the NCP flanking field positions. SAP stands for Sub-Array Pointing.

Field	Beam number	Pointing ( <i>J2000.0</i> )
NCP	SAP000	00 <sup>h</sup> 00 <sup>m</sup> 00 <sup>s</sup> +90°00′00″
3C61.1	SAP001	02 <sup>h</sup> 00 <sup>m</sup> 00 <sup>s</sup> +86°00′00″
RA 6h flanking field	SAP002	06 <sup>h</sup> 00 <sup>m</sup> 00 <sup>s</sup> +86°00′00″
RA 10h flanking field	SAP003	10 <sup>h</sup> 00 <sup>m</sup> 00 <sup>s</sup> +86°00′00″
RA 14h flanking field	SAP004	14 <sup>h</sup> 00 <sup>m</sup> 00 <sup>s</sup> +86°00′00″
RA 18h flanking field	SAP005	18 <sup>h</sup> 00 <sup>m</sup> 00 <sup>s</sup> +86°00′00″
RA 22h flanking field	SAP006	22 <sup>h</sup> 00 <sup>m</sup> 00 <sup>s</sup> +86°00′00″

**Table B.1.** Four bright radio sources around the position of RA 18h flanking field selected for setting the absolute flux of the sky model.

Source	Position ( <i>J2000.0</i> ) Ra, Dec	Frequency [MHz]	Peak flux [Jy]	Reference
J190401.7+8536	19 <sup>h</sup> 04 <sup>m</sup> 03 <sup>s</sup> +85°36′	118.75	5.069 ± 0.549	Zheng et al. (2016)
6C B184741+851139	18 <sup>h</sup> 37 <sup>m</sup> 12.220 <sup>s</sup> +85°14′49.40″	151.5	4.09 ± 0.035	Baldwin et al. (1985)
6C B174711+844656	17 <sup>h</sup> 37 <sup>m</sup> 40.83 <sup>s</sup> +84°45′43.9″	151.5	4.56 ± 0.035	Baldwin et al. (1985)
6C B163113+855559	16 <sup>h</sup> 19 <sup>m</sup> 40.62 <sup>s</sup> +85°49′21.2″	151.5	6.2 ± 0.035	Baldwin et al. (1985)

**Table B.2.** Summary of the CLEAN component model and its clustering.

Cluster	Position ( <i>J2000.0</i> ) RA [hour], Dec [deg]	Number of sources	Maximum flux [Jy]	Total flux density [Jy]	Maximum separation [deg]
1	13 <sup>h</sup> 46 <sup>m</sup> 06.446 <sup>s</sup> +85°30′02.564″	212	5.185	71.87	2.134
2	15 <sup>h</sup> 38 <sup>m</sup> 57.775 <sup>s</sup> +86°46′08.711″	205	6.400	61.51	1.343
3	16 <sup>h</sup> 44 <sup>m</sup> 56.439 <sup>s</sup> +82°00′46.566″	157	4.060	52.54	1.394
4	17 <sup>h</sup> 46 <sup>m</sup> 29.922 <sup>s</sup> +85°25′39.948″	218	5.876	49.19	1.268
5	19 <sup>h</sup> 15 <sup>m</sup> 00.497 <sup>s</sup> +84°26′46.767″	153	4.471	48.08	1.267
6	21 <sup>h</sup> 04 <sup>m</sup> 07.835 <sup>s</sup> +84°12′30.181″	152	8.257	47.69	1.570
7	22 <sup>h</sup> 54 <sup>m</sup> 00.975 <sup>s</sup> +88°23′08.218″	238	5.684	45.48	2.149
8	20 <sup>h</sup> 01 <sup>m</sup> 40.512 <sup>s</sup> +85°59′54.030″	184	6.044	43.34	1.397
9	15 <sup>h</sup> 58 <sup>m</sup> 32.933 <sup>s</sup> +84°33′04.712″	196	22.737	41.71	1.364
10	18 <sup>h</sup> 26 <sup>m</sup> 15.815 <sup>s</sup> +87°37′23.340″	220	3.209	38.07	1.502
11	12 <sup>h</sup> 22 <sup>m</sup> 01.146 <sup>s</sup> +88°28′52.985″	246	2.873	37.40	1.850
12	15 <sup>h</sup> 55 <sup>m</sup> 46.173 <sup>s</sup> +81°59′38.825″	147	5.261	35.62	1.776
13	20 <sup>h</sup> 05 <sup>m</sup> 39.918 <sup>s</sup> +83°06′40.170″	119	2.061	33.69	1.286
14	22 <sup>h</sup> 23 <sup>m</sup> 24.174 <sup>s</sup> +86°16′28.896″	186	5.828	29.83	2.521
15	19 <sup>h</sup> 21 <sup>m</sup> 26.177 <sup>s</sup> +82°13′33.547″	95	2.762	25.27	1.489
16	17 <sup>h</sup> 39 <sup>m</sup> 37.842 <sup>s</sup> +82°09′27.905″	106	2.050	22.13	1.053
17	18 <sup>h</sup> 20 <sup>m</sup> 56.808 <sup>s</sup> +83°20′57.184″	150	1.014	21.49	1.097
18	17 <sup>h</sup> 04 <sup>m</sup> 01.348 <sup>s</sup> +83°46′54.388″	155	2.962	21.04	1.173
19	15 <sup>h</sup> 08 <sup>m</sup> 22.540 <sup>s</sup> +83°36′40.085″	166	2.361	20.83	1.440
20	18 <sup>h</sup> 31 <sup>m</sup> 11.244 <sup>s</sup> +81°33′30.857″	84	2.125	19.51	1.250



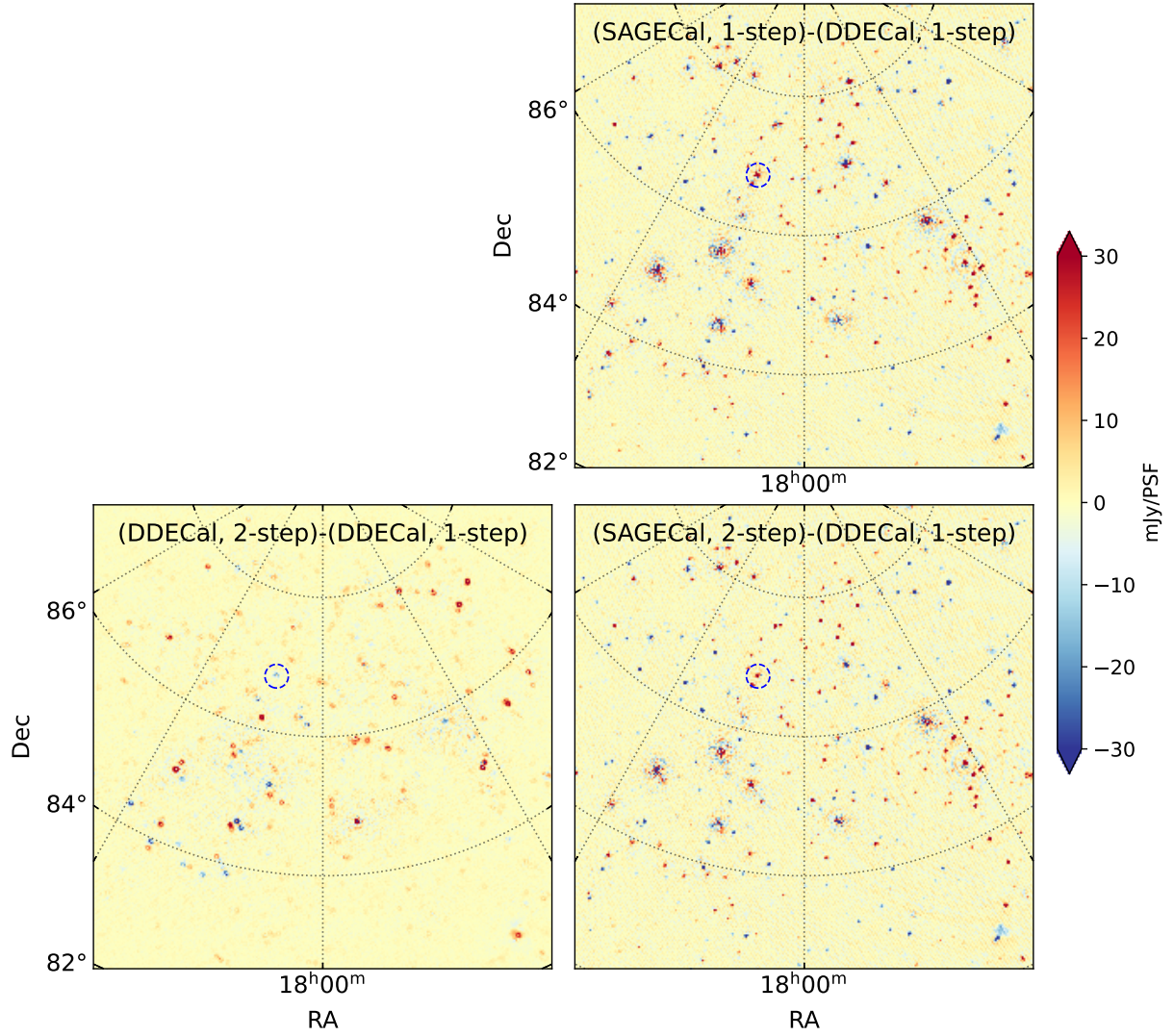


**Fig. C.1.** Difference of LOFAR-HBA  $5^\circ \times 5^\circ$  Stokes-I residual images after DD-calibration with different calibration scenarios on the RA 18h flanking field at frequency 113.9-127.1 MHz shown in Fig. 4. The images are created with a pixel size of 0.2 arcmin using baselines 50 – 5000 $\lambda$ , combining 69 sub-bands and a single observation night L612832 ( $\sim 11.6$ -hour). The residual images with different DD-calibration scenarios are subtracted by the residual image of the DDECal and 1-step scenario. We mark a reference source with a dashed blue circle which is identical to the one in Fig. 4 to compare different DD-calibration residuals.

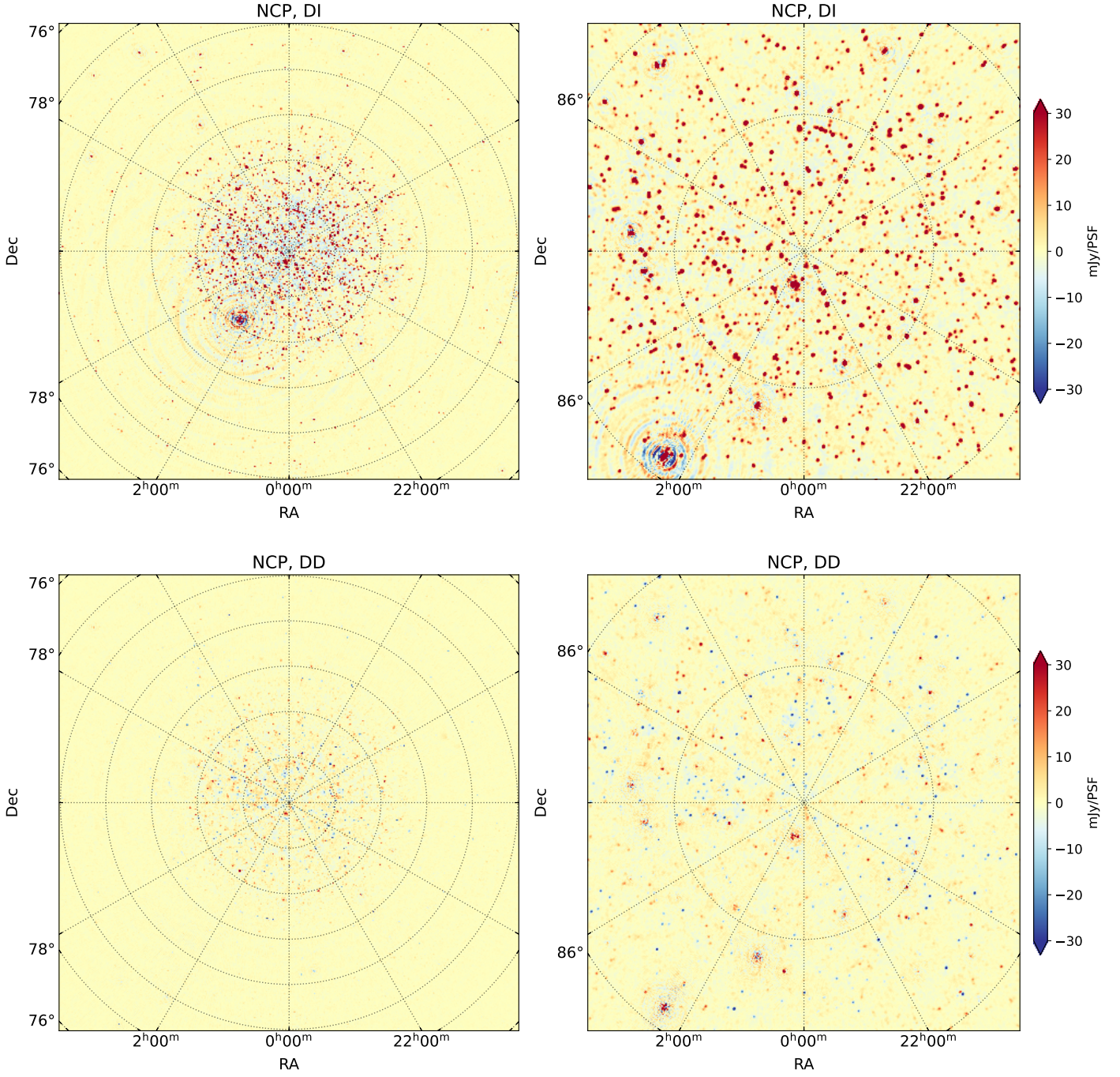


**Fig. D.1.** LOFAR-HBA Stokes-I images of the NCP at frequency 113.9 - 127.1 MHz. All 69 sub-bands are combined for imaging after the DI-calibration (in the top row) and DD-calibration (in the bottom row). The DI and DD-calibrations are performed by SAGECAL and the images are deconvolved by WSCLEAN. **Left column:** A  $20^\circ \times 20^\circ$  image with a pixel size of 0.8 arcmin with baselines between 50-1000 $\lambda$  after DI-calibration (on top) and after DD-calibration (on bottom). **Right column:** A zoomed  $4^\circ \times 4^\circ$  image with a pixel size of 0.2 arcmin with baselines between 50-5000 $\lambda$  after DI-calibration (on top) and after DD-calibration (on bottom).



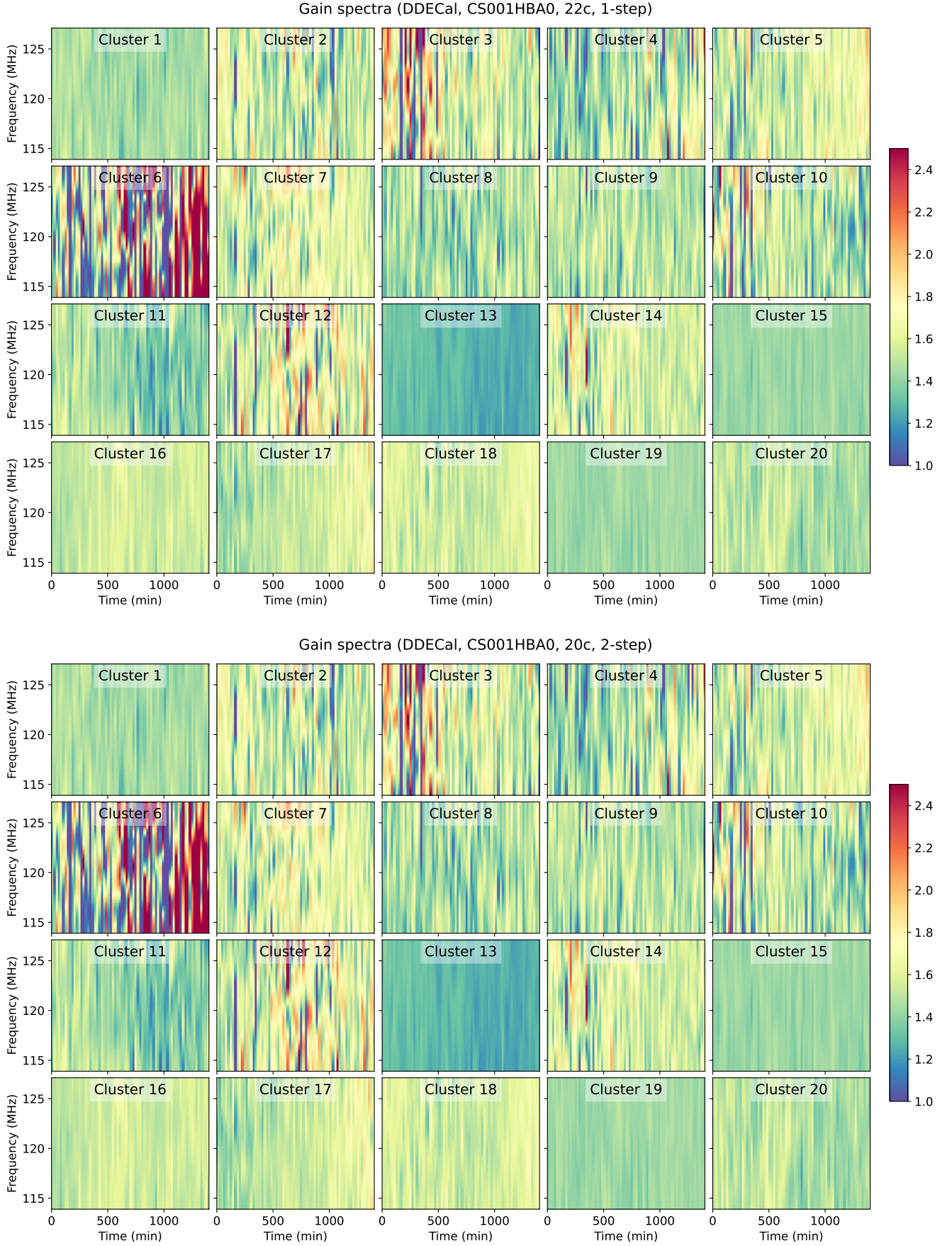


**Fig. E.1.** Gain dynamic spectra obtained by DDECAL algorithm for 20 clusters around the phase centre, using the 1-step method (on top) and 2-step method (on bottom) for one station (CS001HBA0). Different polarisation components are added in quadrature.

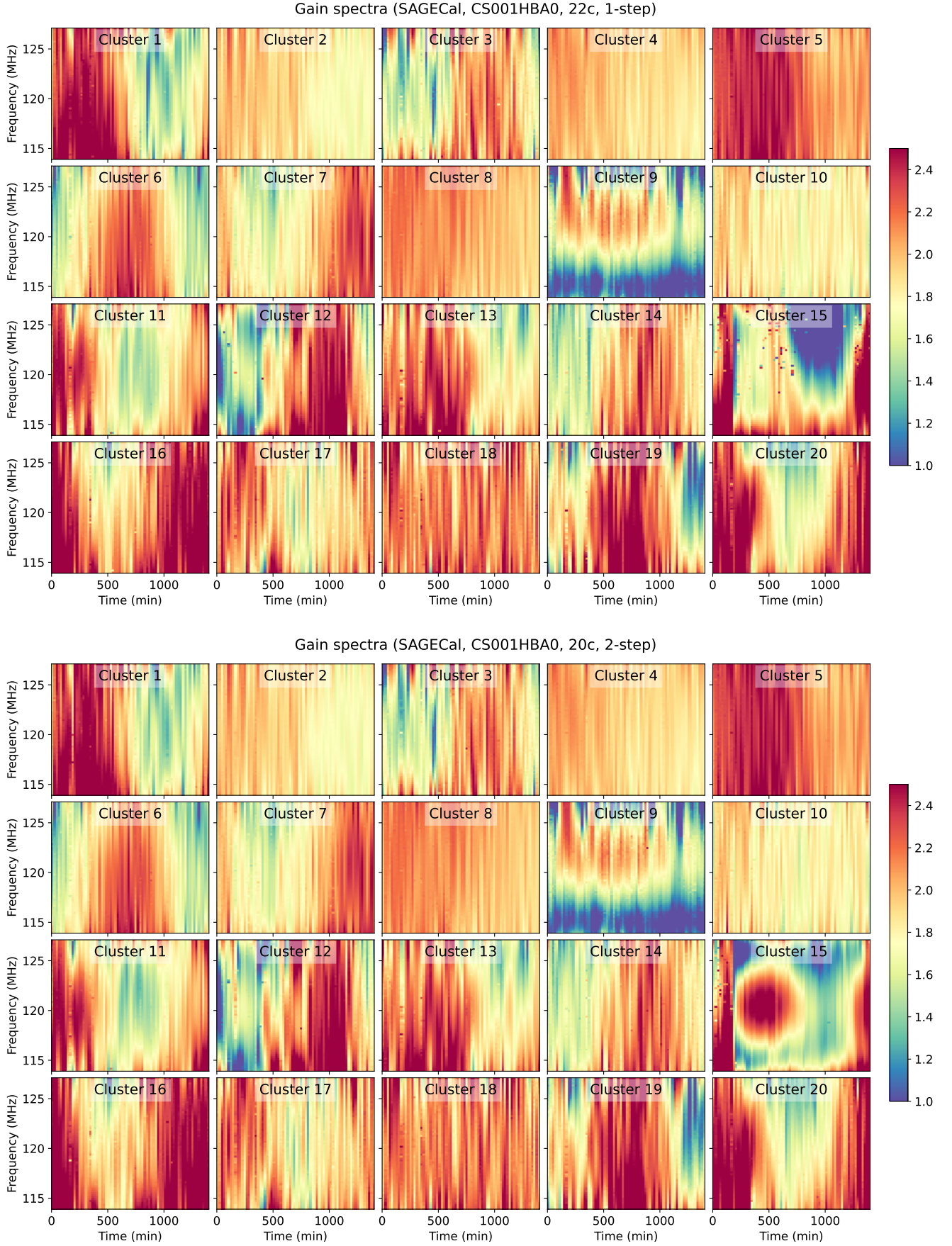


**Fig. E.2.** Gain dynamic spectra obtained by SAGECAL algorithm for 20 clusters around the phase centre, using the 1-step method (on top) and 2-step method (on bottom) for one station (CS001HBA0). Different polarisation components are added in quadrature.

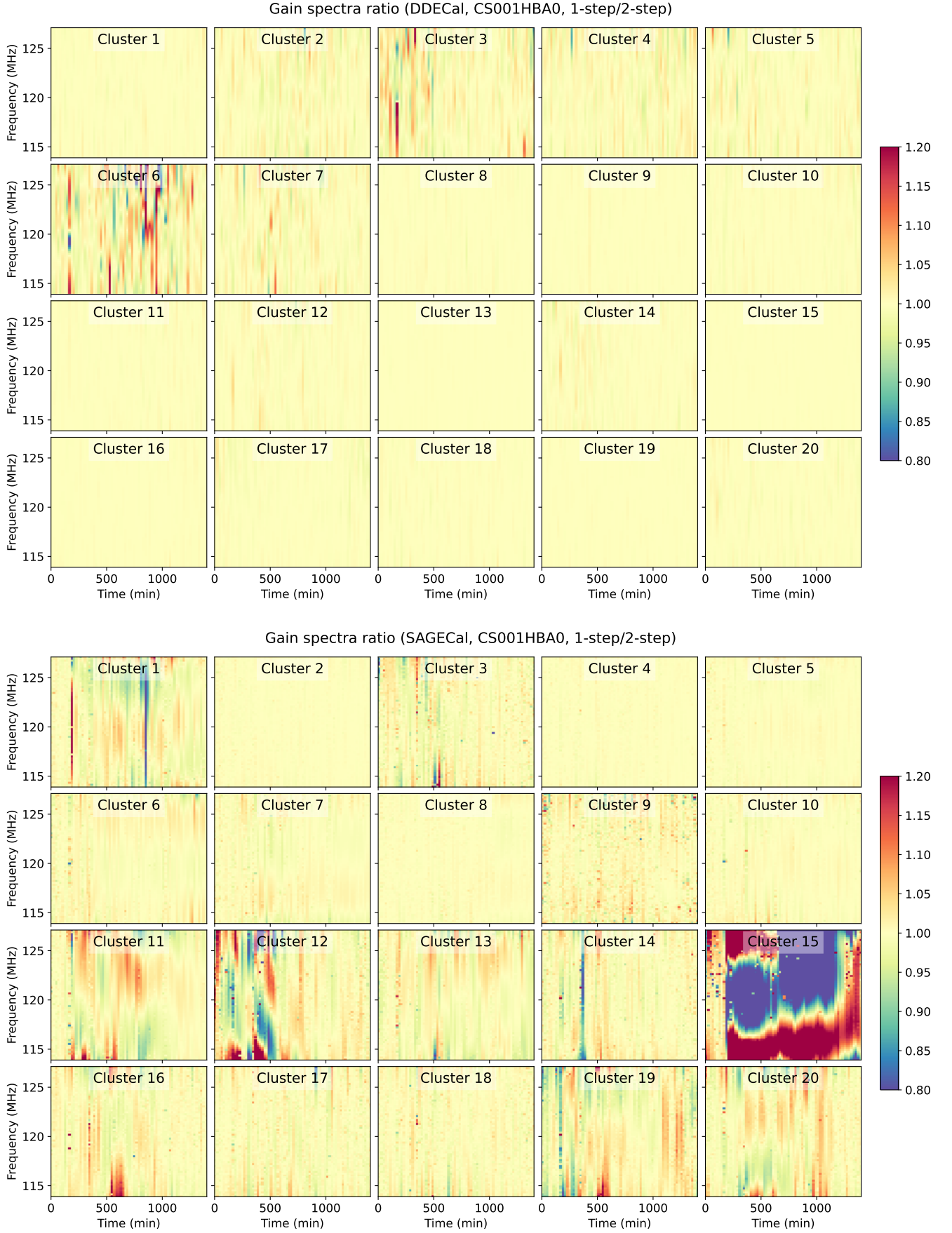


**Fig. E.3.** Ratio of gain dynamic spectra between the 1-step and 2-step methods for 20 clusters around the phase centre for one station (CS001HBA0), obtained by DDECAL algorithm (on top) and SAGECAL algorithm (on bottom). Different polarisation components are added in quadrature. While gain differences between the 1-step and 2-step methods are more prominent in the phase centre for DDECAL (in cluster 2-7 on top), the difference is more obvious outside the phase centre for SAGECAL (in cluster 11-20 on bottom).

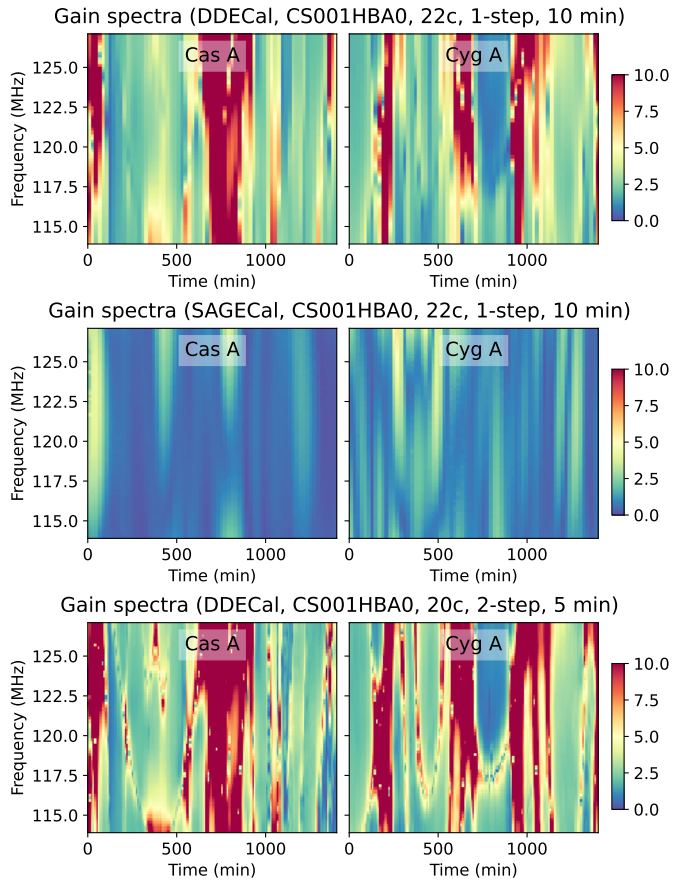


**Fig. E.4.** Gain spectra of Cas A (left) and Cyg A (right) obtained by different calibration strategies for one station (CS001HBA0). Different polarisation components are added in quadrature.